Stellar Masses of Star Forming Galaxies in Clusters

Solohery Mampionona Randriamampandry

Abstract

We determine the stellar mass of star forming galaxies in the X-ray luminous cluster MS 0451.6-0305 at $z \sim 0.54$. The stellar masses are estimated from fitting model spectral energy distributions (SEDs) to deep, optical UBRIz observations obtained from WIYN 3.5m telescope and public NIR K-band image from Palomar Observatory telescope. The model SEDs are based on the stellar population synthesis (SPS) model of Bruzual & Charlot (2003) and Conroy et al. (2009) that span a wide range of age, star formation history, Initial Mass Function (IMF), metallicity and dust content. We measure stellar masses for galaxies down to $M_* \sim 2 \times 10^8 M_\odot$. We find a tight correlation between stellar masses derived from the two SPSs. We compare the derived stellar masses to the dynamical masses for a set of 25 star forming galaxies. The dynamical masses are derived from high resolution, spectroscopic observations of emission lines from the DEIMOS spectrograph on the Keck telescope. A strong correlation is seen between the dynamical and stellar mass for the galaxies; and the star forming galaxies show fairly constant ratio between stellar and dynamical mass. When comparing to the field sample of Guzmán et al. (2003) of luminous compact blue galaxies, we see an excess of low mass galaxies in the cluster.
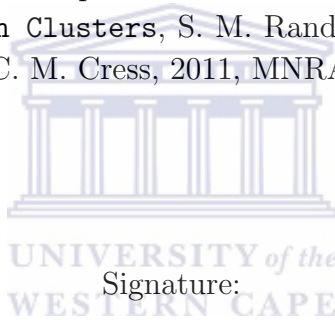
Declaration

I hereby declare that *Stellar Masses of Star Forming Galaxies in Clusters* is my own work, that it has not been submitted for any degree or examination in any other university, and that all the sources I have used or quoted have been indicated and acknowledged by means of complete references.

This work was conducted from July 2009 to November 2010 under the supervision of Dr. Steven Crawford at the South African Astronomical Observatory, Cape Town, South Africa.

A compact version of the thesis is presented in the following paper: `Stellar Masses of Star Forming Galaxies in Clusters`, S. M. Randriamampandry, S. M. Crawford, G. D. Wirth, M. A. Bershady, C. M. Cress, 2011, MNRAS, in preparation.

Signature:

Solohery M. Randriamampandry

November 2010, Cape Town

Acknowledgments

Contents

List of Figures

List of Tables

Chapter **1**

Introduction

Star formation activity plays a significant role in the evolution of galaxies and understanding the decrease in the total star formation rate is an important topic in modern cosmology (Heavens et al. 2004). Galaxy clusters, the largest gravitationally bound structures in our universe, are ideal laboratories to study the evolution of star formation as function of its physical environment and galaxy population (Bohringer & Werner 2010).

The first evidence for galaxy evolution was seen in clusters; the increasing fraction of blue galaxies at higher redshift (Butcher & Oemler 1978). In the past decades, a number of galaxy evolution studies have been focused on the Butcher & Oemler (BO) effect at various wavelengths; for instance in the mid-infrared recent works have confirmed the existence of the BO effect for massive galaxy clusters at moderate redshift (Saintonge et al. 2008; Haines et al. 2009). However, many of the details of galaxy evolution in these large scale structures remain to be understood.

It is, therefore, important to further explore such clusters at intermediate redshift (see eg: Moran et al. 2006, 2007) in order to determine the properties of galaxies such as ages, metallicities, star formation histories, and stellar populations. In this work, we investigate the physical properties of galaxies residing in a cluster. We derive the stellar and dynamical mass for a sample of 25 star forming galaxies, and we compare our results to the sample of field galaxies at the same redshift from previous work.

This introductory chapter presents the background of the growing field of research in star forming galaxies residing in galaxy clusters. In particular, we include a brief introduction of Luminous Compact Blue Galaxies; an overview of the observations of galaxy clusters and the evolution of large scale structure; and various properties of intermediate redshift galaxy cluster MS 0451.6-0305. Finally, we discuss the most common method for measuring stellar and dynamical masses of galaxies.

1.1 Star Forming Galaxies

A galaxy is a collection of stars that is gravitationally bound together; it mainly contains stars, gas, dust and dark matter. Most of the stars contained in galaxies are less massive than $20M_\odot$. Stars are hot, massive, dense gas spheres emitting radiation produced in their center from nuclear reactions and gravitational contraction. They contain gases and

chemical elements, and are primarily composed of hydrogen and helium. The physical properties of stars can be studied via spectroscopic observations that provides details about their temperature and composition.

1.1.1 Star Formation

Formation of stars occurs inside relatively dense concentrations of interstellar gas and dust called molecular clouds. These regions are extremely cold, temperature ~ 10 to 20K and commonly composed of CO and H_2 molecules (Kitsionas 2003). Stars form from the molecular clouds within the densest regions of the interstellar medium (ISM). The study of star formation is quite a complex matter, which involves many diverse processes and phenomena (McKee & Ostriker 2007). There are a few major distinct triggering mechanisms that are commonly discussed. The accumulation of gas into a dense ridge that collapses gravitationally into dense cores, the density enhancements in a cloud, and also the collision of clouds (Elmegreen 1997).

The study of the ISM is important for understanding star formation since giant molecular clouds are the precursors to the star formation process. The ISM plays a major role in the star formation process because of its intermediate role between stellar and galactic scales. The ISM is made of mixture of gas in all states: atoms, molecules, ions, and dust grains that spread across the interstellar space. The gas and dust contribute respectively about 99% and 1% of the total mass of the interstellar medium. The chemical elements in the gas phase consist of roughly about 89% hydrogen and 9% helium and 2% elements heavier than hydrogen (Kitsionas 2003).

Starburst galaxies are galaxies undergoing tremendous star formation where the ratio of its rate to the normal SFR is typically much higher. They are typically forming stars 10-20 $M_\odot$ per year (Pérez-Gallego et al. 2010). Starburst galaxies have large gas supplies and are rich in HI (Garland et al. 2004,2005); they emit significant far infrared and radio fluxes. They are typically blue galaxies that have morphological types of spirals, and irregulars, and they are usually in interacting and merging galaxies (Garland et al. 2007; Pérez-Gallego et al. 2010). Starbursts are believed to be common, but temporary, events throughout the universe that alter the structure of the host galaxies. Example of star-bursting galaxies are: Blue Compact Galaxies (BCGs), Luminous Compact Blue Galaxies (LCBGs), Blue Compact Dwarf Galaxies (BCDGs), Luminous Infrared Galaxies (LIRGs), Ultra-luminous Infrared Galaxies (ULIRGs).

1.1.2 Luminous Compact Blue Galaxies (LCBGs)

LCBGs have small half light radii, high surface brightness, emit detectable radio continuum flux, have high Hα luminosities, and are metal poor indicating strong star formation properties (Werk et al. 2004). They are characterized by high luminosity $M_B < -18.5$, blue intrinsic color B-V < 0.6 and particularly high surface brightness $\mu_e < 21$ mag arcsec^{-2} (Phillips et al. 1997; Crawford et al. 2006; Pisano et al. 2007; Hoyos et al. 2008). This morphological class of galaxies are quite rare and they are often not found in the local universe (Pisano et al. 2007).

The population of LCBGs belongs to a mixture of star-bursts that dominates at $0.3 < z < 1.0$ and their present-day identity is still-unknown (Guzman et al. 2003, Crawford et al. 2004, Noeske at al. 2006). It is also argued that LCBGs are just a common stage in the evolution of galaxies and not a distinct class of galaxy (Hammer et al. 2001). At intermediate redshift and up to $z \sim 1$, LCBGs have a high number density and are known to contribute up to 45% of the star formation density in the universe (Guzmán et al. 1997).

LCBGs are rapidly evolving galaxies which implies that they play an important role in the evolution of the star formation history of the universe at moderate redshift (Guzmán et al. 1997). The mechanisms driving the evolution are not yet fully understood. However, it is believed that LCBGs will evolve into either massive dwarf elliptical or dwarf irregular or likely to be low-mass late-type spiral galaxies (Phillips et al. 1997; Pisano et al. 2007, 2009). LCBGs have been suggested to be the progenitors of present-day clusters spheroidal galaxies (Guzmám et al 1996; Koo et al. 1997). Despite their high luminosities, LCBGs have dynamical masses consistent with low-mass galaxies such as dwarf elliptical, irregulars, and low luminosity spirals. The velocity dispersion and the resolved profile show that the systems cannot be too far out of equilibrium (Bershady et al. 2004). LCBGs lie at the extreme end of a fairly continuous distribution of normal star-forming galaxies so they are not really isolated as compared to the normal star-forming galaxies (Werk et al. 2004).

1.1.3 Major Science with LCBGs

In cosmological timescales, LCBGs play a significant role in our understanding of galaxy evolution. Many authors have recently highlighted various sciences done with LCGBs (Guzmán 1997, 2003), some major results found are:

- LCBGs have evolved more than any other galaxy class in the last ~ 8 Gyrs.

- They are a major contributor to the observed enhancement of the star formation rate density of the universe at z $\leq$ 1.

- They may be lower-mass counterparts of the recently discovered star forming galaxies at z $\sim$ 3.

- Some LCBGs at z $\leq$ 1 are candidates to be the progenitors of today's spheroidal galaxies.

1.2 Galaxy Clusters

Observations of Galaxy Populations in Clusters

The first evolution seen in galaxy clusters was the increase in the number of blue galaxies with redshift (Butcher & Oemler 1978). Thus far, many cluster surveys have revolutionized our understanding of the environmental effect upon the evolution of galaxies (Sato & Martin 2006; Moran et al. 2007). Elliptical and S0 galaxies are found to reside in the cluster core while spirals live in the outer parts (Butcher & Oemler, 1978).

The physical properties of a galaxy such as luminosities, morphologies, star formation rates and nuclear activity are affected by the environment that it inhabits. In both the core and in the outskirts of the cluster the mean star formation rate shows a continuous correlation with local galaxy density (Poggianti et al. 2008). This correlation is important since it clarified some of morphological and environmental differences observed between galaxy in cluster and the field.

The environmental dependence on star formation history (SFH), masses and morphologies is also described by two well known relations of morphology-density and star formation-density. The morphology-density relationship states that rich galaxy systems have greater fraction of bright giant elliptical (Dressler et al. 1997). The star formation density relationship describes that galaxies in the low dense environement have higher mean star formation rate than galaxies in the high density regime (Deng 2010). In clusters, evolution seen in galaxies is known to be driven by local galaxy density environment (Sato & Martin 2006). Galaxies in cluster evolve differently than field galaxies due to the physical processes in the dense environment such as galaxy harassment, mergers, and interaction with the intra-cluster medium (Moran et al. 2007). Differences between cluster and field populations can be used to explore how physical processes affect the evolution of a galaxy as a function of its environment.
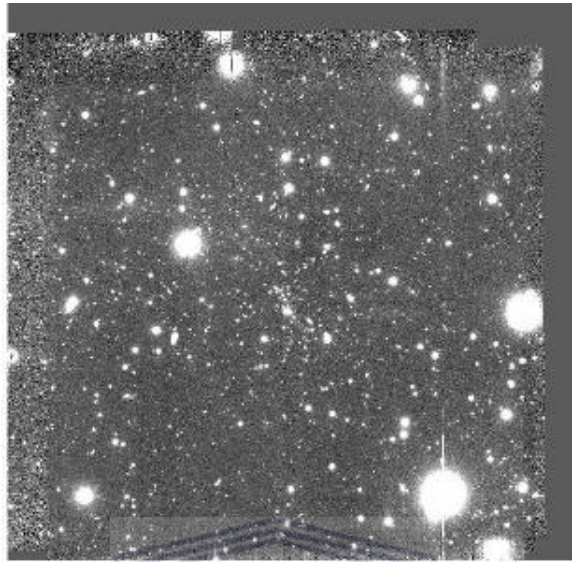
Figure 1.1: R-band imaging of MS0451.6-0305 cluster taken from WIYN[1] 3.5m telescope (Crawford et al. 2006).

1.3 Galaxy cluster MS 0451.6-0305

The Galaxy cluster MS 0451.6-0305 was discovered as part of Einstein Observatory Extended Medium Sensitivity Survey (EMSS). The EMSS is a collection of serendipitous X-ray sources detected with the Imaging Proportional Counter (IPC) on board the Einstein Observatory. The IPC field of view is $\sim$ 1 square degree with exposure times ranging from $\sim$ 800 to $\sim$ 40 000 s (Giacconi et al. 1979; Gioia et al. 1987, 1990). The sample consists of 835 sources resulting from the analysis of 778 square degree of the high galactic latitude sky $|b| \geq 20°$. The X-ray fluxes of the survey are in the sensitivities range 10^{-13} - 10^{-12} ergs cm^{-2} s^{-1} in the 0.3 - 3.5 keV energy band (Gioia et al. 1988, 1990). MS 0451.6-0305 is the most X-ray luminous, distant and rich cluster in the EMSS (Gioia et al. 1994). The basic properties of the cluster are summarized in Table 1.1.

This cluster has long been studied in near-IR and optical photometric and spectroscopic surveys (Stanford et al. 2002). This massive, luminous and cosmologically significant X-ray cluster has been studied in X-ray (Jeltema et al. 2001, Donahue et al. 2003), in submillimetre (Borys et al. 2004), in the optical (Gioia 1994; Crawford et al. 2009) and radio wavelengths (Wardlow et al. 2010; Alba et al. 2010).

Table 1.1: Properties of MS0451 cluster at z = 0.538 (Crawford et al. 2009).

R.A. (h.m.s.)[1]	Decl. (d.m.s.)[2]	Rvir (Mpc)	R_{200} (Mpc)	M_{200} (M$\odot$)	σ (km s^{-1})	L_X (L$\odot$)
04 54 10.8	-03 00 56	2.6	1.64	1.4×10^{15}	1354	3.8×10^{11}

J2000: [1] Hours, minutes, and seconds; [2] Degrees, arc-minutes, and arc-seconds.
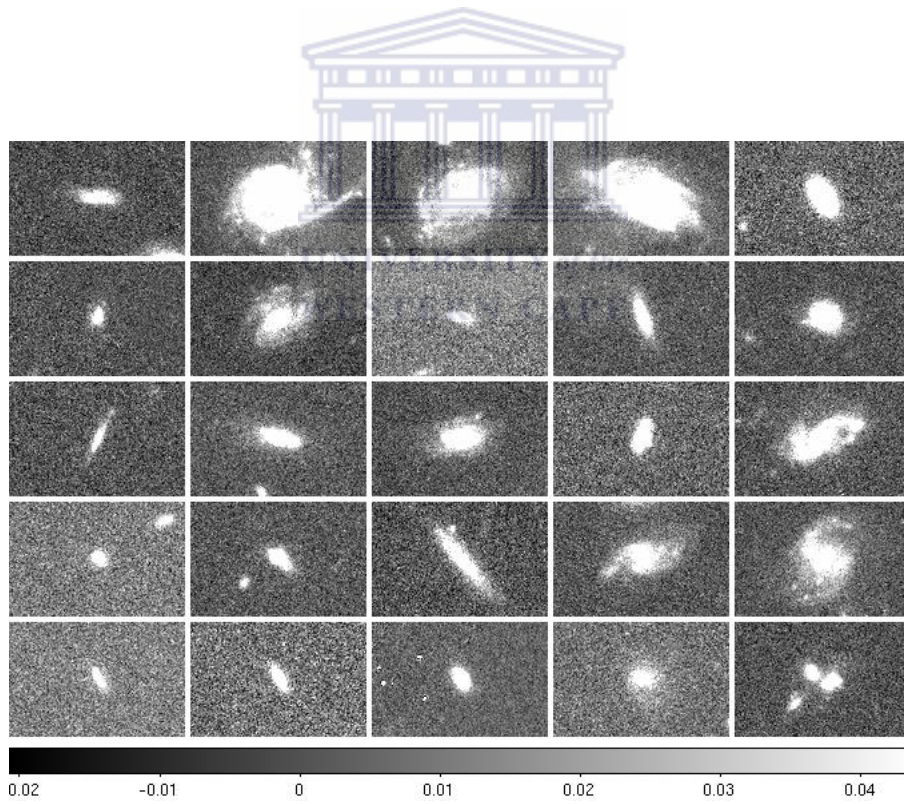
Figure 1.2: Montage of MS 0451 cluster members from deep optical images UBRIz observed with HST. Figure of 25 galaxies that have different morphologies are displayed.
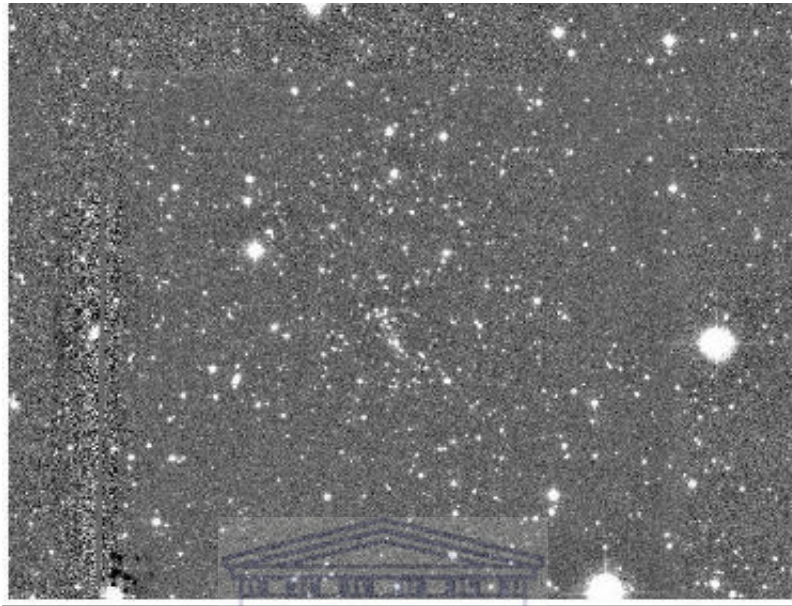
Figure 1.3: K-band imaging of MS0451.6-0305 cluster taken from the Hale 200 inch telescope at Palomar[2] (Moran et al. 2007).

1.4 Galaxy Mass Measurement

1.4.1 Stellar Mass Measurement

The stellar mass of galaxies is commonly derived via spectral energy distribution (SED) fitting. This method compares the broad-band photometric magnitudes with the synthetic SED template. Bundy et al. (2009) estimated the stellar mass by SED fitting where the observed SED of each galaxy is compared to a grid of 24800 models from Bruzual & Charlot (2003) stellar population synthesis code that spans a wide range of metallicity, exponential SFR history at ages (roughly less than the age of the universe) including different IMF and dust content. The physical properties of galaxies for instance stellar mass, color and morphology has been the main focus of more recent work eg: Bundy et al. (2009)

IR observations are less biased by star formation, and thus serve as a better tracer of the underlying stellar mass in galaxies (Bundy et al. 2004). The K-band image is a better tracer of old stellar populations and plays a significant role in probing dusty star-forming regions (Brinchmann & Ellis 2000). Stellar masses of galaxies can be calculated from the

K-band (NIR) photometry for $z \leq 1.5$ (Bundy et al. 2006).

The study of the most active phases of the SFH of galaxies and tracking their growing stellar masses may help towards understanding galaxies formation. Galaxy masses are important in galaxy evolution study since they would link the theories of galaxy formation and observations of the galaxy population (van der Wel et al. 2006). Galaxy dynamical mass can be derived from the rotation curves and velocity widths (Pérez-Gallego et al. 2010).

Stellar mass estimates provide a snapshot of the star formation history and measurement of the galaxy baryonic mass for a galaxy while dynamical mass measurements provide an excellent tracer of the underlying dark matter halo. Investigation of the correlation between stellar mass and age is also useful.

Stellar mass measurements have been used in a wide range of studies including Brinchmann & Ellis (2000), Guzmán et al. (2003), Bundy et al. (2005, 2006, 2009) with some of relevant studies to this work.

Spectral Energy Distributions

The spectral energy distribution (SED) is defined as the same as spectrum but the spectrum is not always calibrated to give physical units of energy. The SEDs are used to characterize astronomical objects by plotting the flux versus wavelength. It describes how much energy the source emits as a function of wavelength. It is often calibrated using standard magnitudes system such as Vega and AB system.

There are two methods for computing the spectral energy distribution (SED) model of a galaxy. In the first method, one has to model the stellar spectra library and then linearly combine individual stellar spectra to construct a galaxy spectrum (Faber 1972, Pickles 1985). The second method is based on adjustments of few parameters including the stellar initial mass function (IMF) and star formation rate (SFR). This technique is known as the evolutionary population synthesis (Bruzual & Charlot 1993, Maraston 1998). For simplicity, in most cases the simple stellar population (SSP) theory is often considered. In this approach, it is assumed that stars are formed at the same time, with distribution in mass given by one chosen initial mass function (IMF), and with identical chemical composition.

The IMF is an important input parameter of stellar population synthesis models. It describes the fraction of stars born per unit logarithmic mass interval (Scalo 1986) i.e the initial distribution in mass along the main sequence. There are two well known ingredients used to build the SEDs of SSPs: the isochrone synthesis and fuel consumption theory. The word isochrone is defined as the location of stars with the same age in the

Hertzsprung-Russel diagram.

In the first approach, the total flux is computed by integrating the spectra of all stars along the isochrone (Charlot & Bruzual 1991). However, since isochrones are calculated in discrete steps in time, the isochrone synthesis method has limitation due to insufficient time-steps performed; eg: stellar evolution of TP-AGB branch stars. The second technique uses fuel consumption, so the fuel (mostly hydrogen and helium) is integrated along the evolutionary track. This is based on the idea that the luminosity of luminous stars in the post-main sequence should be directly linked to the fuel available to stars at the turn off mass (Maraston 1998, 2005).

1.4.2 Dynamical Mass Measurements

The spectroscopic features such as [OII]3727, Hβ and [OIII]5007 emission lines can be used to measure dynamical mass. It can also be derived from the kinematics of the gas, as given by the velocity dispersion (σ) of rest-frame optical lines (Phillips et al. 1997). The method used to measure the dynamical mass in this study is similar to the Virial mass estimation used by (eg: Guzmán et al. 1996; Phillips et al. 1997) in which M $\simeq$ $\frac{3c_2\sigma^2 R_e}{G}$ where $c_2 \simeq 1.6$ is a geometry-dependent factor (Bender et al. 1992), and R_e half light radius.

1.4.3 Comparison of Mass Measurements

The amount of dark matter present in a galaxy is found to increase as function of galaxy's luminosity and size (Padmanabhan et al. 2003). Non-baryonic matter includes the so called dark matter that has unusual or dark behavior; the word dark might not literally indicate a lack of light but might show an absence of scientific knowledge about this matter. It is neither emitting significant electromagnetic radiation nor interacting with matter beyond gravitation attraction. Its existence can be revealed via its gravitational attraction using the weak-lensing method (Bartelmann 2010), the dynamics of galaxies, cosmic microwave background observation, and evolution of clustering.

Assuming that the difference between stellar and dynamical mass is the fraction of dark matter present in galaxies (Padmanabhan et al. 2003). The derived stellar mass generally represents the baryonic mass of the galaxy (Drory et al. 2004). Studies of the relationship between stellar and dynamical mass have shown a tight correlation of the form given by $M_{dyn} = (M_*)^\alpha$ where $\alpha = 1.28 \pm 0.03$ (Bundy et al. (2007); see also: Padmanabhan et al. 2003; Drory et al. 2004). The early type galaxies, massive and old,

are often assumed to be dark matter dominated thus this relationship will be $M_{dyn} \gg M_*$ and for baryon dominated $M_{dyn} \geq M_*$ (Rettura et al 2006).

Bundy et al. (2007) investigate the relation between dynamical and stellar mass that explores trends seen in the dynamical mass functions that match to those previous estimates of stellar mass functions by Bundy et al. (2005). They found that galaxies with large stellar mass evolve predominantly into spheroidal by $z \leq 1$ (Bundy et al. 2007). Comparison between stellar and dynamical mass may serve as a good estimates of the fraction of dark matter content of the galaxy. Furthermore, as shown by de Jong & Bell (2006), it also provides constraints on the mass normalization of the stellar population model.

In this work, we compare our calculated masses to the results on mass measurements for a field sample of LCBGs at intermediate redshift presented in Guzmán et al. (2003). They fit the observed photometry to the two component galaxy population model made up of SFR history of a burst component and an underlying exponential declining. The stellar mass measurements by Guzmán et al. (2003) are similar to the Brinchmann & Ellis (2000) method except that they redshift-ed all the models. They found that the stellar mass of LCBGs is ten times smaller than today galaxies. And the comparison of masses shows that the derived medium stellar mass is twice smaller than the derived mass from Virial mass (Guzman et al. 2003).

1.4.4   Evolution in Galaxy Mass

It has been known that more massive galaxies have formed their stars earlier and over a short period of time while less massive galaxies formed their stars later but most efficiently over a long duration (Cowie et al. 1996; Heavens et al. 2004; Cattaneo et al. 2008). The shift of threshold mass of star formation from massive galaxies to low-mass galaxies has been coined by Cowie et al. (1996) as downsizing.

There is a significant difference in star formation history for massive and less massive systems. This mass limit plays a big role both triggering and quenching star formation in galaxies depending on galaxy masses and its stellar mass content. The key mechanisms responsible for evolution trends seen in galaxies would be constrained by quantifying the downsizing, and testing it as function of environment dependence (Bundy et al. 2006).

1.5 Plan of the Thesis

A number of physical processes are known to drive evolution of galaxies in cluster (Moran et al. 2007) but the effectiveness of many of these processes are related to the environment of the galaxy. Understanding of these processes are important for a complete picture of galaxy evolution. Determining the physical differences between cluster and field galaxies allows an exploration of how these transformative phenomenon effect galaxy evolution as a function of environment.

The major aim of the thesis is to estimate and compare the stellar and dynamical mass of star forming galaxies in intermediate redshift galaxy clusters and the field. This thesis is structured as follows:

Chapter 2 deals with observations and analysis performed including matching the seeing between different images, object detection and extraction, photometry using SExtractor, a summary of a previous analysis done, sample selection, as well as description of the correction for galactic extinction and calculation for photometric upper limit.

Chapter 3 shows detailed procedures and results of spectral energy distribution fitting, a detailed algorithm to calculate the stellar masses including a review of stellar population synthesis, a summary of the library model utilized and a Monte Carlo error analysis.

Chapter 4 presents results and comparison of stellar masses estimates, and a discussion on models, masses and galaxy properties.

Chapter 5 and Chapter 6 provide our dynamical masses measurements, comparisons of stellar and dynamical masses for the field and cluster sample, discussions of the results, conclusions, and a call for further work. Throughout this thesis, we adopt $H_0 = 71$ km s^{-1} Mpc^{-1}, $\Omega_{(m)} = 0.27$ and $\Omega_{(DE)} = 0.73$.

Chapter 2

Data & Analysis

This Chapter presents a summary of the optical and near-infrared observations used and the basic analysis performed in this study. In Section 2.1, we describe the observations obtained of the cluster. In Section 2.2 and Section 2.3, the seeing convolving and object detection are given. In Section 2.4, photometry measurements via SExtractor are presented. We finally provide a brief outline of the procedures applied for sample selection and the extinction correction in Section 2.4.1 and Subsection 2.4.2.

2.1 Observations

We utilize deep optical UBRIz imaging of MS0451.6-0305 cluster (MS0451, hereafter) that were obtained between 1999 October and 2004 June, with the WIYN[1] 3.5m telescope's Mini-Mosaic Camera; 0".14 per pixel and $9'.6 \times 9'.6$ field of view. Full details of the observations are presented in Crawford et al. (2009).

For the near-infrared observations, we use archive data from Moran et al. (2007). K_s-band observations was taken with the WIRC camera on the Hale 200 inch telescope at Palomar[2] Observatory. The seeing ranged from 0.6" to 1" for imaging during the observing runs (Moran et al. 2007). Within the 3σ depth, Moran et al. (2007) provided optical–NIR photometry catalog that have measurement for upper magnitude limit of 20.2 mag. in K_s-band. Both dataset were processed for basic reduction and mosaic-ed into deep images and we refer to the original papers for further detail on these steps.

2.2 Creating Seeing Matched Images

From the ground, the shape of stars is dominated by seeing. When we look at a radial plot, the light distribution is well described by a Gaussian profile. To perform accurate photometry on all of the images, we convolved each image to the worse seeing. We match the seeing between the ground based optical and near-infrared images and calculate σ_{image}. The Gaussian's profile parameter σ_{image} is related to the Full Width and Half Maximum (FWHM) by:

$$\mathrm{FWHM} = 2.354 \times \sigma_{\mathrm{image}}$$

Table 2.1: Values of FWHM, σ, σ_{ker} and Zero-points.

Band	FWHM	σ	σ_{ker}	Zero-points
U	7.67	3.26	2.10	31.25
B	6.90	2.93	2.54	32.30
R	5.29	2.25	3.16	32.58
I	5.53	2.35	3.09	31.95
z	7.52	3.20	2.19	31.63
K	9.14	3.88	N/A	27.82

The values of σ_{image} are compared for each image, and near infrared K-band imaging was identified to have the largest value of σ_{image}; which is the σ_{worse}.

We measured the size of the kernel to match the optical images to the worse seeing by calculating σ_{kernel}:

$$\sigma_{\text{worse}}^2 = \sigma_{\text{image}}^2 + \sigma_{\text{kernel}}^2$$

The values of σ_{ker} are presented in Table 2.1 and used into the IRAF task gauss to degrade all the optical imaging to match the worst seeing.

2.3 Object Detection and Extraction

We performed both object detection and extraction on SExtractor via R-band imaging. The archival K-band imaging was aligned to the optical UBRIz frame via geomap in IRAF task. Here we provide a brief description of our calibration for the optimal value of detection parameters for SExtractor.

We investigated detection parameters of measurement such as DETECT$_{\text{MINAREA}}$, DETECT$_{\text{THRESH}}$, ANALYSIS$_{\text{THRESH}}$, DEBLEND$_{\text{NTHRESH}}$ and DEBLEND$_{\text{MINCONT}}$ for SExtractor to test for objects detection and extraction parameters. First, the detection DETECT$_{\text{MINAREA}}$ parameter that determines the minimum number of pixels above the threshold required to be considered an object (i.e to be detected above the background). Next, the detection threshold DETECT$_{\text{THRESH}}$ parameter which determines the level from which SExtractor should start treating pixels as if they were part of objects, it is dependent on the minimum number of pixels as specified by DETECT$_{\text{MINAREA}}$. The DETECT$_{\text{THRESH}}$ is in units of background standard deviation (σ). ANALYSIS$_{\text{THRESH}}$ is defined as the same as DETECT$_{\text{THRESH}}$ but with respect to what objects to extract for

photometry. Finally, the DEBLEND$_{\text{NTHRESH}}$ is a parameter that SExtractor uses to split light into different objects based on pixels above DETECT$_{\text{THRESH}}$.

We determine the best value for DETECT$_{\text{MINAREA}}$ and DETECT$_{\text{THRESH}}$ through visual inspection and average counts of objects detected. Our analysis yielded the following values: DETECT$_{\text{MINAREA}} = 10$; i.e sources are extracted where a minimum of 10 contiguous pixels and DETECT$_{\text{THRESH}} = 3$ and ANALYSIS$_{\text{THRESH}} = 1.5$. We adjust the contrast parameter for deblending to DEBLEND$_{\text{MINCONT}} = 0.005$, and DEBLEND$_{\text{NTHRESH}} = 32$. These parameters were all determined in such a way that we can detect the majority of objects but minimizes the noise objects.

Combination of these therefore has excluded any double objects detected at the same aperture and provided an optimal average counts of objects extracted. We therefore have selected the primary cluster members that have medium brightness; which are not saturated nor too faint to be confused: $18 \leq m \leq 23$, $8 \leq FWHM \leq 11$. This is a refined catalog that finally used to calculate the average FWHM.

These parameters are plugged in to SExtractor to produce a preliminary photometric catalog. The output contains coordinates of objects, aperture magnitude and Full Width and Half Maximum (FWHM). We also performed a cutoff of the useless sources in the boarder of the images; $500 \leq x \leq 4500$, $500 \leq y \leq 4500$ pixels, and selected objects in the central region.

2.4 Photometry

Photometry was measured using SExtractor (Bertin & Arnouts 1996). We use SExtractor in two-image mode with source detection performed on the R-band images. The Zeropoints for magnitude measurements as supplied by Crawford et al. (2006) and Moran et al. (2007) are listed in Table 2.1 for each band. Our catalog includes photometry from all optical near infrared data of 3σ depths. This final photometric catalog for measurements from six filters contains coordinates, magnitudes and their uncertainties.

2.4.1 Sample Selection

The final representative sample was selected through several steps. The primary sample contains 785 selected cluster objects across the central region of the imaging; $500 \leq x \leq 4500$, $500 \leq y \leq 4500$. Next, we selected 292 cluster objects as galaxies with a redshift between $0.5 < z < 0.58$. Our final sample is drawn from star forming cluster objects identified from deep spectroscopic imaging (Wirth et al. 2010). For the present work, we

were able to extract and investigate a final representative sample of 25 galaxies. These objects are spectroscopically confirmed members of the cluster and identified as starbursting galaxies; known as Luminous Compact Blue Galaxies (Crawford et al. 2006).

2.4.2 Correction for Extinction

The emitted light from galaxies in MS0451 will be absorbed and scattered along the way by the interstellar gas and dust in the galactic plane. Due to galactic extinction from our galaxy, the flux in each passband needs to be corrected for dust extinction. Cardelli et al. (1989) has unified the mean extinction law from near infrared through optical to UV by means of a relationship which depends only on single parameter. There are different models that fit and correct for extinction for a given galactic latitudes (see eg: Tarantola & Valette 1982; Ochen et al. 1998). However, we applied a common technique of subtracting off the values supplied by the Nasa Extragalactic Database (NED). Based on the full sky map of Schlegel et al. (1998), the value of $A_V = 0.143$ for MS0451 where A_V is the normalization of the extinction curve. The extinction across the wavebands value or color excesses of E(B-V) = 0.033.

2.5 Galaxy colors

Analysis of this sample of 292 cluster objects was undertaken in previous work by us during the Honours project. The investigation of galaxy colors and magnitudes was aimed to further focus on the evolution of the properties of these galaxies. It was carried out by comparing our observed spectra to the Spectral Energy Distributions (SEDs) model to estimate the masses and ages of cluster members where all models have been redshift-ed to the cluster redshift. For this study, we have focused on how the age and mass of galaxies evolve across our sample. We have used GALAXEV (BC03) to create SEDs using the simple stellar populations (SSPs) model to extract model ages and masses.

The color-color diagrams (CCD) over-plotted with the model tracks show the difference range of age in Gyr. As can be seen from Figure 2.1, our data sample is well-fitted by the model tracks. Galaxies are spread over 0.1 Gyr, 1.01 Gyr up to 5 Gyr; with the oldest galaxies being red. The color-magnitude diagram (CMD) over-plotted with the model tracks in Figure 2.2 shows the different range of stellar mass in $M_\odot$. The mass ranges from 10^8 $M_\odot$ to 10^{11} $M_\odot$. From the shape of these tracks, it seems as if our sample has low-mass galaxies which are actively star-forming galaxies. The K-band luminosity is significantly important for probing older stellar populations and would be insensitive
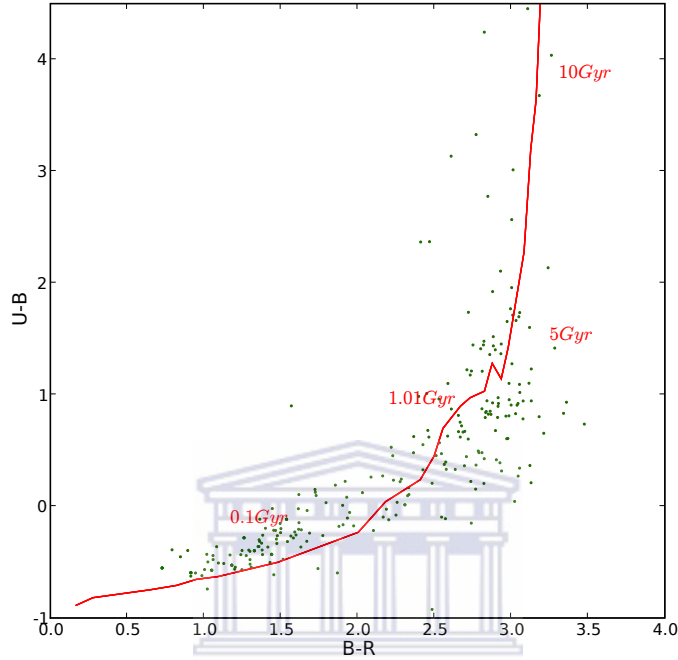
Figure 2.1: (U-B) color vs. (B-R) color over-plotted with the model track

to the previous star formation history (Brinchmann & Ellis 2000). In Figure 2.2 its importance can be seen straight from the slope of the mass tracks, as it can be readable horizontally.

We have compared our study to previous analysis by Bundy et al. (2006) and found that massive galaxies tend to be red whereas lower mass galaxies included both blue and red systems. The red, massive galaxies track towards to the red sequence which is not actively star-forming. The blue lower mass galaxies are certainly still forming stars. The lower mass galaxies found at intermediate redshift often have spectra indicative of recent star formation (Tran et al. 2007).

Although, there are two different types of galaxy the so called early-type and late-type galaxies that are related to the galaxy masses and star formation history. Star forming galaxies can be traced by defining a mass limit where the shift of star-forming galaxies from massive; red, early-type galaxies to lower mass; blue, late-type galaxies occurs (Cattaneo et al. 2008). This threshold mass is found to decreases with time. This concept is well-known as downsizing which indicates that more massive galaxies have formed their stars
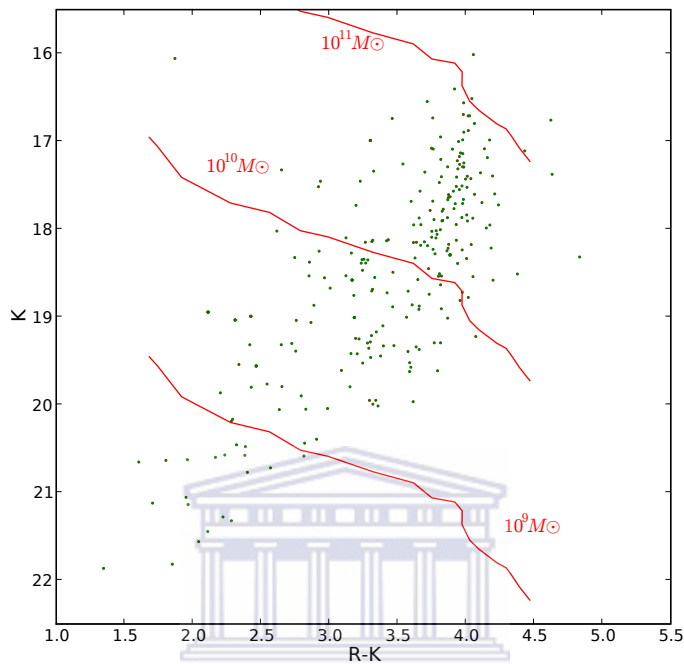
Figure 2.2: K-magnitude vs. (R-K) color plotted together with the model track.

earlier and over a short periods while lower mass galaxies are known to have formed their stars most efficiently at later times and over a longer periods (Cowie et al. 1996; Bundy et al. 2006). We explored these phenomena by computing a SED model. However, we did not make any investigation in what mechanisms drive a downsizing. We stress that the assumptions made in the computed SEDs would not provide enough information of star formation history. Those may also yield large uncertainties in terms of age, metallicity and mass. Using more detailed star formation history for the SEDs model is of interest for the present work.

In summary, we investigated the colors of 292 spectroscopically confirmed members of the galaxy cluster MS0451 at a redshift of z = 0.54. We compare the color-magnitude and color-color diagrams of the cluster to a model of SEDs from Bruzual and Charlot (2003). Analysis of the color magnitude diagrams show a deficit of massive blue galaxies as compared to red galaxies, similar to the downsizing effect seen in the field.

2.6 Calculating Upper Limits

Due to the faint K-band magnitudes for some sources, we explored the effects due to detection limits on our photometry. Calculation of upper limit was determined from the limiting magnitude value ($K_s = 20.2$) from Moran et al. (2007). We plot the magnitudes along with its uncertainties when both values do not exceed the upper limit otherwise its upper limit will be plotted to stand as representative of it; see figures in Section 3.5. We do not update the actual value of magnitude and its associated error in the optical-NIR catalog. However these sources do have very large error values. Therefore, analysis of $\chi^2_{\min}$ may not provide accurate information since it was derived from fitting of six point - fluxes that includes K-band.

---

[1]The WIYN Observatory is a joint astronomical facility of the University of Wisconsin-Madison, Indiana University, Yale University, and the National Optical Astronomy Observatory.

[2]The Palomar Observatory is an astronomical facility located in north San Diego County, California, USA

Chapter **3**

Method

The stellar population synthesis (SPS) models are tools for interpreting the integrated light such as colors, line indices, and continuum that we observe from galaxies. The recent SPS codes have more advanced ways for computing SED parameters including ages, metallicities and SFHs. These codes simulate physical properties of a galaxy including metallicity, dust and star formation histories for a given age of a galaxy.

It is preferred to have synthetic galaxy SEDs templates because they can mimic both early and late phases of galaxy evolution (Massarotti et al. 2001). So how are SEDs model made? The SEDs of galaxies are created by adding various type of stellar SEDs together. The SEDs model are basically designed to match the observed galaxies SEDs by making some assumptions about the number of different relationship of types of stars. In SED fitting, the physical properties of galaxies such as star formation histories (SFHs), metallicity, age and mass can be derived by comparing the observed spectra to the stellar population models (Walcher et al. 2010).

In Section 3.1, we provide literature review on Stellar Population Synthesis (SPS) model of Bruzual & Charlot (2003) (hereafter, BC03) and Conroy et al. (2009) (hereafter, CN09). Section 3.2 presents the ingredients for both software including, a brief summary on stellar evolution, initial mass function (IMF), metallicity, and comparison of their features and limitations. Section 3.3 discusses the effectiveness of our two large computed SEDs libraries and the correction applied for dust extinction. In Section 3.4, we show the detailed derivation of all equations utilized to infer the stellar masses. Section 3.5 and Section 3.6 present the best-fit figures and error analysis using Monte Carlo simulation applied for all of our sources, respectively.

3.1 Stellar Population Synthesis

The SPS models have been used to predict the observed SEDs of galaxies based on a number of ingredients. The major parameters incorporated in SPSs model include stellar evolution prescription, initial mass function (IMF), dust content, and the stellar SEDs libraries that are used to describe the properties of stars at any position in the Hertzsprung-Russell (HR) diagram. The SPS codes are tools frequently utilized for galaxy evolution studies to constrain physical properties of galaxies such as stellar mass, mean

age, metallicity, and star formation history (Conroy et al. 2009; Kriek et al. 2010).

Uncertainty in stellar evolution models limit the effectiveness of SPS codes. Especially problematic are aspects of stellar evolution modeling of the asymptotic giant branch (AGB) (Carbon and Oxygen-rich stars, cool giants stars T$\lesssim$ 4000K, lifetime $\sim$1 Myr), thermally pulsating asymptotic giant branch (TP-AGB), blue stragglers (BSs), horizontal branch (HBs) stars, and binary stars system (Bruzual & Charlot 2003; Kriek et al. 2010). The TP-AGB stellar phase are difficult to model because of convective overshooting in stellar tracks (Maraston et al. 2006). The evolution of stars in this phase is unpredictable and not fully understood due to strong mass loss. Therefore, there are still substantial amount of work to be performed to further understand the theory of stellar evolution in these stages. They also suffer from the logarithmic slope of IMF at the main sequence (MS) turn-off since the IMF Salpeter power law is found to be mass-dependant, and, not universal (Bastian et al. 2010). Furthermore, the effects of age and metallicity in the evolutionary population synthesis produce degeneracies in the SPSs (Bruzual & Charlot, 2003). This is difficult to quantify since increasing age at fixed metallicity has similar effect as increasing metallicity at fixed age.

3.2 SPS Software Models

3.2.1   GALAXEV

GALAXEV is a software for computing the spectral evolution of stellar populations for galaxies released in 2003 by Bruzual & Charlot. The SEDs are produced in two modes which include two different resolutions. The high resolution mode covers a wavelength (λ) range from 3200 to 9500 Å at a resolution of 3 Å. Its low resolution counterpart has λ from 91 Å to 160μ with wavelength sampling of 1221 points per spectrum. Both high and low resolution share a wide range of ages from 1×10^5 to 2×10^{10} yr. The simple stellar populations (SSPs) parameters includes ages, metallicities, Padova 1995 evolutionary tracks within mass ranges at lower and upper mass cutoffs of 0.1 and 100 $M_\odot$ respectively. These SSPs are normalized to a total mass of $1M_\odot$ and have zeropoints computed in the Vega magnitude system. GALAXEV uses a new library of observed stellar SEDs predictions called STELIB assembled by Le Borgne et al (2003) where the fundamental stellar parameters across the HR diagram were optimized. The library of observed stellar spectra is used to map the theoretical isochrones in the HR diagram i.e for any given properties of stellar populations, any SFH can be expanded in a series of instantaneous star bursts (SSP), and is suitable for the purpose of population synthesis modeling.

Bruzual & Charlot (2003) have shown that their model can reproduce the observed optical and NIR color magnitude diagram (CMD) of Galactic star clusters of various ages and metallicities. They have compared this model to a number of observations of star clusters. The spectral fit can constrain physical parameters such as metallicity, SFH and dust content of galaxies. Bruzual & Charlot (2003) have also tested GALAXEV and found that it can reproduce in detail the typical galaxy spectra extracted from the SDSS Early Data Release by Stoughton et al. (2002).

Furthermore, GALAXEV is one of the first model to enable accurate studies of absorption line features over all ages that reproduce simultaneously well the observed strengths of those Lick indices at that epoch (Bruzual & Charlot, 2003). Thus it offers the possibility to explore new indices over the full λ range from 3200 to 9500 Å. For star forming galaxies studies, the attenuation of starlight by dust can be included in the modeling (Bruzual & Charlot, 2003).

3.2.2   Flexible SPS

Flexible SPS (FSPS) code of Conroy et al. (2009) is designed to compute galaxies SED models. The software is a collection of Fortran routines, which is highly flexible to handle various uncertainties in many aspects of stellar evolution such as the TP-AGB stars, HB stars, BSs stars and IMF. Conroy et al. have taken into account all the systematic uncertainties that affect the derived physical properties of galaxies such as stellar mass, age, metallicity, and SFR (Conroy et al. 2009a).

FSPS has been utilized to fit the broad-band near-UV through NIR photometry to estimate stellar masses via Markov Chain Monte Carlo (MCMC) method for a representative sample of galaxies at low (z = 0) and high redshift (z = 2) with uncertainties in derived masses of 0.3 and 0.6 dex respectively when uncertainties in stellar evolution is included. For the TP-AGB phase treatment in the stellar evolution, two parameters have been strongly accounted for, the bolometric luminosity and effective temperature and can be arbitrary modified (Conroy et al., 2009). The variables $\triangle T$ and $\triangle L$ are introduced; which is the shift in effective temperature $\log(T_{eff})$ and bolometric luminosity $\log(L_{bol})$ with respect to the default evolutionary tracks of TP-AGB stars in the HR diagram respectively . They adopt an optimistic estimate for these variables to -0.1< $\triangle T$ < 0.1 and -0.2< $\triangle T$ < 0.2 (Conroy et al. 2009, 2010). The idea is motivated by the fact that there is a lack of observational constraints for these parameters, thus it is very difficult to even specify a reasonable prior range for these parameters.

The logarithmic slope of the IMF implies on uncertainty of 0.4 mag per unit redshift in the K-band leading to a substantial source of error in the luminosity evolving sys-

tem. The range of parameters for FSPS was defined to be larger than that suggested by observational results for instance metallicity distribution function, HB morphology, BS specific frequency. It is shown that broad band photometry is not sensitive to these uncertainties within that parameter range (Conroy et al., 2009). For star-forming galaxies, the TP-AGB phase and dust attenuation lead to substantial systematic uncertainties in UV, optical and NIR colors both from stellar evolution and dust at different ages. The assumed dust model distribution law also contribute to these uncertainties (Conroy et al. 2010), although, the uncertainties in color come dominantly from stellar evolution such as in the treatment of TP-AGB, BS, and morphology of the HB. The logarithmic slope of the IMF for passive galaxies is lower that introduces less affect on uncertainty than star-forming galaxies; the same IMF may introduce different uncertainties. Thus it is very important to take account the detailed sources of uncertainty because the small systematic uncertainties in the model will substantially affect the interpretation of the derived physical properties (Conroy et al., 2009).

3.2.3   Software Comparison

FSPS has an improved treatment of TP-AGB phase since Conroy et al. (2009) modified the isochrone synthesis of Padova while GALAXEV has not. GALAXEV and FSPS have been tested and performed well with Magellanic Cloud (MC) data at all ages. At low metallicity and old ages, all models colors UBVRIJHK are in agreement within an error 0.05 mag (Conroy et al. 2010). Spectral indices of Milky Way (MW) stars clusters are well fit by both FSPS and GALAXEV. FSPS also fit UV photometry data of MW, M87, M31 star clusters well because both post-AGB and HB evolutionary phase are handled flexible while GALAXEV performed less well because of their incomplete treatment of these advanced evolutionary phase (Conroy et al. 2010b). Comparison to ugrzYJHK photometry of massive red sequence galaxies indicate that FSPS and GALAXEV generally performed well (Conroy et al. 2010b). Optical spectral indices of massive galaxies are generally well fit by the FSPS and GALAXEV models with prediction of excess of D_n4000 and $H_{\delta A}$ strengths too weak compared to red massive galaxies (Conroy et al. 2010a).

FSPS and GALAXEV reproduced well the optical and near-IR colors of post-burst galaxies while for instance, as a comparison to other SPS, Maraston et al. (2005) (M05) cannot because of its color is too red and of the incorrect age-dependence. These galaxies contain a large proportion of intermediate age stars between 0.5 and 2 Gyr and should provide an unique constraint on the importance of TP-AGB stars in galaxies. GALAXEV and M05 both failed in the far-UV and near-UV respectively. In summary, for many color magnitude diagram (CMD) FSPS performed well. However, SPS are primary tested for

star clusters that have more old populations and metal rich (TP-AGB stars are rare in individual star clusters), galaxy studies may suffer significantly due to lack of accurate calibration (Conroy et al. 2009a).

3.3 Library of SED Models

In the SED models, the effects of metallicity and dust extinction play a big role as they can be used to estimate how young the stars are and also to determine the main features in some emission and absorption lines (Bruzual & Charlot, 2003). Here we briefly summarize how we compute the SED libraries from the two codes in this work. We computed two large libraries of SEDs from the SPS code of Bruzual & Charlot (2003) and Conroy et al. (2009) respectively at high and low resolution of wavelength. The two libraries are more or less constructed to have input parameters as similar as possible. The grid of ingredients that span a wide range of age, metallicity, SFH and dust extinction, are shown in Table 3.1 and Table 3.2.

3.3.1 Bruzual & Charlot (2003)

We provide a summary of the procedures for creating galaxy SEDs from GALAXEV as follows:

- convert the SSPs in ASCII format into binary files using ascii_ised program.

- input the binary files to composite stellar population `csp` alias task and generate multi-components SFHs that include CSPs and SSPs.

- we compute CSPs of burst length and exponential with e-folding time of 0.5 to 2.0 Gyr in step of 0.5.

- we similarly compute constant SFH of 0.5 to 2.0 in unit of $M\odot$ yr^{-1} in step of 0.5.

- to extract individual SED at any age (in Gyr), input SSPs and CSPs binary files to galaxevpl `gpl` alias task

- we repeat the above steps for each single metallicity of 0.005, 0.02, 0.2, 0.4, 1 and 2.5.

Based on various input parameters that are summarized in Table 3.1, a large library of SEDs model computed from GALAXEV was generated. This includes SSPs of the

Table 3.1: Input grid for BC03 SEDs library

Parameter	Range
Age (Total = 34) (Gyr)	From 0.001 up to 14.0
Burst SFR (Gyr)	Burst length = 0.0, 0.5, 1.0, 1.5, 2.0
Expo SFR (Gyr)	τ = 0.5, 1.0, 1.5, 2.0
Const SFR (M$\odot$yr^{-1})	Const = 0.5, 1.0, 1.5, 2.0
IMF	Salpeter, HR from Padova 1994
Metallicity ($Z\odot$)	0.005, 0.02, 0.2, 0.4, 1 and 2.5
E(B-V) (mag)	0, 0.1, 0.25, 0.5, 1
Extinction law	MW and Calzetti et al. (2000)

same ages for both models at six different metallicities. We use Padova (1994) tracks with initial mass function (IMF) of Salpeter at high resolution of wide wavelength range. These are used to create SEDs for a total number of 34 ages at unequally spaced time steps from 0.001 to 14 Gyr. These contain burst and exponential SFHs at of 0.5 to 2.0 Gys of 0.5 age step and likewise for constant SFHs in M$\odot$ yr^{-1}. We then redden the SEDs via Milky Way and Calzetti (2000) extinction law for five values of excess color, thus in total the final number of SEDs in the library are 28800.

3.3.2 Conroy et al. (2009)

For purpose of conformity with SEDs created from GALAXEV, we use Salpeter IMF and assigned an appropriate range of predefined metallicity for SSPs and CSPs. Similarly to Section 3.3.1, we provide a summary of the procedures for creating galaxy SEDs from FSPS as follows:

- generate SEDs model from FSPS code via autosps.exe or `sps` alias task

- during computation, two files supposed to have been created: one containing spectra and another storing magnitudes at different filters, both files are heading with the following four quantities log(age), log(mass), Log(L$_{\text{bol}}$) and log(SFR) along with 72 outputs of SED at different ages.

Note that wavelength data are stored in a separate file, they are all identical over the computed fluxes. Ages of spectra are in unit of Log$_{10}$(yr), thus one must convert them to

Table 3.2: Grid for library spectra model of CN09

Parameter	Range
Age (Total = 72)(Gyr)	0.0003 up to 14.0
Burst SFR (Gyr)	Burst length= 0.0, 0.5, 1.0, 1.5, 2.0
Expo SFR (Gyr)	$\tau = 0.5, 1.0, 1.5, 2.0$
Const SFR (M$\odot$yr^{-1})	Const = 0.5, 1.0
IMF	Salpeter LR
Metallicity ($Z\odot$)	0.025, 0.05, 0.2, 0.4, 1, 1.6
E(B-V) (mag)	0, 0.1, 0.25, 0.5, 1
Extinction law	MW and Calzetti et al. (2000)

Gyr. Again for purpose of similarity to BC03, fluxes derived from FSPS are in units of L$_\odot$ Hz^{-1} which were converted to cgs system in erg s^{-1} cm^{-2} Å^{-1} by computing the following term $3\times10^{18} \times \dfrac{F}{\lambda^2}$. The flux in each single age contains 1221 lines of sampling points that has to be extracted and converted. We handle the conversion with python script that extracts these SEDs. The code splits the header mentioned above from spectra then load each single spectral and put its corresponding wavelength together with its converted flux. For all ages either SSP or CSP, one go computation of IMF, SFH and Z is sufficient. We have verified the consistency of both SEDs priory to any further detailed analysis.

Based on various input parameters that are summarized in Table 3.2, a large library of SEDs model computed from FSPS was created. The SEDs model created here come from seventy two ages of six metallicity with ten different SFHs for CSPs plus seventy two ages of six metallicity for SSPs. In fact, SFHs with burst length and exponential with e-folding time of 0.5 to 2.0 Gys of 0.5 age step and for constant SFH of 0.5 and 1.0 in M$_\odot$ yr^{-1} were computed. The SSPs have seventy two ages of six metallicity for SSPs. Thus after reddening, there are 47520 SEDs in this library.

3.3.3 Spectra Reddening

The effects of galactic extinction on the flux of bluer passband might be quite significant. Thus it is common to correct for that by assuming an appropriate dust extinction law. In our stellar mass calculations, Calzetti et al. (2000) starburst attenuation law is used

to account for dust extinction. The Milky Way dust curves is also utilized for extinction correction (Cardelli et al. 1989). For each dust curve, we assigned E(B-V) values as listed in Table 3.1 and Table 3.2. These two extinction laws produce very small differences (Papovich et al. 2001). For comparison, the best-fit values of E(B - V) from the SED modeling differ at $\sim$ 20-30% see Table 3.3; where we have also summarized our SED fitting results that include metallicity, ages and amount of dust from BC03 and CN09, respectively.

Table 3.3: Results of SED fitting

Obj	z	ID	$Z(Z_\odot)$	Age(Gyr)	E(B-V)	$Z(Z_\odot)$	Age(Gyr)	E(B-V)
00	0.5315	1081	1.000	0.070	0.50	1.000	0.075	0.50
01	0.5271	1093	0.400	0.010	1.00	0.100	0.048	1.00
02	0.5321	1118	0.400	0.500	1.00	0.025	1.284	1.00
03	0.5299	1178	1.000	12.00	0.10	0.100	0.524	1.00
04	0.5388	1252	1.000	1.000	0.25	1.000	2.334	0.25
05	0.5309	1348	0.400	0.050	0.25	1.000	0.064	0.25
06	0.5677	1462	1.000	0.112	0.25	0.400	0.070	0.50
07	0.5422	1669	1.000	0.070	0.10	1.000	0.075	0.10
08	0.5285	1954	0.005	13.00	0.10	1.000	0.101	0.50
09	0.5440	1968	1.000	0.080	0.25	0.400	0.953	0.10
10	0.5133	2045	0.005	1.000	0.10	1.000	0.707	0.10
11	0.5478	2084	2.500	1.500	0.10	0.025	0.335	1.00
12	0.5297	2224	1.000	0.100	0.50	0.025	0.087	1.00
13	0.5347	2300	2.500	0.044	0.10	1.000	0.031	0.25
14	0.5258	2312	1.000	0.080	0.50	0.025	0.056	1.00
15	0.5454	2521	0.400	0.080	0.00	1.000	0.070	0.00
16	0.5417	2932	2.500	0.056	0.10	0.400	0.064	0.10
17	0.5366	629	1.000	1.000	0.25	1.000	2.010	0.25
18	0.5381	664	1.000	0.125	0.50	0.025	0.288	0.50
19	0.5512	732	0.400	3.000	0.25	0.100	7.705	0.25
20	0.5381	777	0.005	0.090	0.10	0.400	0.056	0.10
21	0.5482	814	2.500	1.000	0.50	0.100	2.010	0.50
22	0.5401	910	0.200	0.500	0.10	1.000	0.700	0.10
23	0.5313	925	0.005	2.000	0.10	0.025	0.953	0.10
24	0.5319	947	0.200	0.031	0.10	0.200	0.035	0.10

3.4 Procedures & Fitting

We carry out a similar procedures for deriving stellar masses by using the multi-color method of Brinchmann & Ellis (2000). It determines the stellar masses of these galaxies via fitting the SEDs model to observed spectra. Here we provide the steps required to calculate the stellar masses, however, a more detailed description has also been supplied in the main text. In this case, the following are things needed and or steps to be run:

- Optical-NIR magnitude photometry that includes magnitude error.

- Convert the magnitude to point fluxes; we use Vega magnitude system

- Libraries of SEDs that span a wide range of age, metallicity, SFRs etc.

- Compare the observed SEDS to the model SEDs to calculate the different between them.

- Store the constant of normalization in order to scale and generate a stellar mass.

We wrote software that are made up of several modules, which makes the software more flexible. These can easily be exported or imported to different scripts. Chi2.py, readfield.py, filter.py and plotflux.py are Python scripts that calculate the central wavelength of each bandpass then derive the fluxes by normalizing it with the zero-point flux source as defined in Equation 3.3. The main fitting code performed χ^2 calculation; it estimates the constant of normalization and outputs different information for every single object such as object's identification, constant of normalization, minimum value of χ^2 and its best model name. We provide one of our own SEDs fitting software written in python in appendix. We calculated model flux-points by convolving the model flux with the photometric bands and interpolating it to all filters passband within the appropriate central wavelength for a finite range of interval. Model fluxes are shifted by $1 + z$ where z is the redshift of the observed galaxy model SEDs.

In contrast, for a given SEDs library model and list of filter, an observed SED is compared to every single model SED in the library. We applied a chi-square minimization technique to normalize both SEDs and select the best-fit model. The software chi2.py will go through and compare the differences between observed and predicted one and afterwards select its closest model spectra in the library, and outputs a constant of normalization (N). In brief, each object is matched and normalized to a model to derive the best-fit for that object by minimizing the two dimensional error in the data. The stellar masses can then be calculated, after fitting the observed flux-points to those ones derived

from the best fitting model of a given set of template model spectra. Given the luminosity distance D_L at each object redshift z and the stored list of best fit model for each object along with its minimum $\chi^2_{\min}$ value and N, stellar masses can directly be derived (see Section 3.4.3).

3.4.1 Determining flux

This subsection shows the detailed mathematical equations of the codes that includes the full derivation of the main fitting algorithm hereafter in Equation 3.17. We derive the uncertainty $\sigma_{f,(i)}$ and the constant of normalization N in detail as shown in Equation 3.9 and 3.16. We started off by writing down the conversion equation of the observed magnitudes for each ith photometric band into incoming apparent flux $f_{obs,i}(\lambda)$. This is equivalent to reconstruct the SEDs of target galaxies at very low spectral resolution by sampling their luminosity at the effective wavelength of the filters available (Massarotti et al. 2001). The mean flux density in a broad passband is given by:

$$f_\lambda(P) = \frac{\int P(\lambda) f_\lambda(\lambda) \lambda d\lambda}{\int P(\lambda) \lambda d\lambda} \tag{3.1}$$

Where $f_\lambda(\lambda)$ is the flux density of the target galaxy, $P(\lambda)$ is a dimensionless passband or transmission function. The normalized zero-point flux $f_\lambda(P)$ can be evaluated through each passband and central wavelength for all band. We used the spectra of Vega as zero-point spectra.

In our case, for a given optical and near-IR UBRIzK filters, each zero-point flux is different and all must be performed in order to get the apparent flux. The magnitude and the apparent flux is connected as the following.

$$f_{obs,i} = f_\lambda(P) 10^{-0.4 m_i} \tag{3.2}$$

In other notation:

$$f_i = f_{Vega,i} 10^{-0.4 m_i} \tag{3.3}$$

where f_i, $f_{Vega,i}$ and m_i are the observed flux, zero-point flux and magnitude in the ith filter respectively. In each band, we derived the error in flux $\sigma_{f,(i)}$ as shown in the following:

$$m_i = -2.5 \log_{10} f_i + \text{constant}_i \tag{3.4}$$

or

$$m_i = -2.5 \log_{10} \frac{f_i}{f_{Vega,i}} \tag{3.5}$$

The photometric errors of m_i with respect to f_i is given by:

$$\sigma_{m,i}^2 = \left(\frac{\partial m_i}{\partial f_i}\right)^2 \sigma_{f_i}^2 \tag{3.6}$$

with

$$\ln x \approx 2.3 \log_{10} x$$

Thus

$$\sigma_{m,i}^2 \approx (1.087)^2 \times \frac{\sigma_{f,i}^2}{f_i^2} \tag{3.7}$$

$$\sigma_{f_i}^2 = \left(\frac{\sigma_{m,i}}{1.087}\right)^2 f_i^2 \tag{3.8}$$

Therefore, for each band i:

$$\sigma_{f,(i)} \approx \left(\frac{\sigma_{m,i}}{1.087}\right) f_i \tag{3.9}$$

3.4.2 Determining χ^2

The χ^2 measures how well the colors of the template spectrum match the colors of the observed galaxy, modulo the photometric uncertainty σ_i. The constant of normalization N scales and summarizes the discrepancy between the observed and model galaxy spectrum. In χ^2 weighted least-squares minimization technique, any galaxy observed fluxes, SEDs are compared to spectra model as given by:

$$\chi^2(z) = \sum_{i=1}^{n_{filters}} \left[\frac{F_{obs,i}(z) - N \times F_{model,i}(z)}{\sigma_i} \right]^2 \tag{3.10}$$

where $F_{obs,i}(z)$ $F_{model,i}(z, params)$ and σ_i are the observed and model of fluxes and the variance of the observation in the ith band respectively, and N is a normalization constant. We derive analytically the constant of normalization N as follows:

$$\frac{\partial \chi^2}{\partial (z, params)} = 0$$

$$\Longleftrightarrow$$

$$\frac{\partial \chi^2}{\partial N} = 0$$

$$2 \times \sum_{i} \frac{(F_{obs,i} - N \times F_{model,i}) \times (-F_{model,i})}{\sigma_i^2} = 0 \tag{3.11}$$

$$N \times \sum_{i} \frac{[F_{model,i} \times F_{model,i}]}{\sigma_i^2} = \sum_{i} \frac{[F_{obs,i} \times F_{model,i}]}{\sigma_i^2} \tag{3.12}$$

Thus

$$N = \frac{\sum_{i} \frac{[F_{obs,i} \times F_{model,i}]}{\sigma_i^2}}{\sum_{i} \frac{[F_{model,i} \times F_{model,i}]}{\sigma_i^2}} \tag{3.13}$$

3.4.3 Calculating the Stellar Mass

Given various physical properties for instance bolometric magnitude $\log(L_{bol})$, star formation rate $\log(SFR)$ and arbitrary model masses $\log(M_m)$ at different ages from the model fitting results. For a given a luminosity distance (D_L), and from the relationship between flux and luminosity of an astronomical body, the M_* is derived as follows.

$$Flux = Constant \times Luminosity \text{ (i.e } F = N \times L)$$

$$F = \frac{L}{4\pi \times D_L^2} \tag{3.14}$$

Let us write M and L with subscript notation m i.e the mass M and luminosity L that have been generated from SPS. Stellar masses are determined by scaling the model mass-to-light-ratio to the K-band luminosity.

$$M_* = \frac{M_m}{L_m} \times L$$

where L is the luminosity (in $L\odot$) and the latter equation is equivalent to:

$$\frac{L}{L\odot} = \frac{M_*}{M_m} \times L_m$$

where M_* is the stellar mass and M_m is a model mass generated by the SPS after normalizing the observed and model SED.

Thus,

$$F_m = \frac{M_* \times L_\odot}{4\pi \times D_L^2 \times M_m} \times L_m \qquad (3.15)$$

since

$$F = N \times L$$

Therefore,

$$N = \frac{M_* \times L_\odot}{4\pi \times D_L^2 \times M_m} \qquad (3.16)$$

Finally,

$$M_* = \frac{4\pi \times D_L^2 \times N \times M_m}{L_\odot} \qquad (3.17)$$

3.5 Fitting & Plots

The SEDs model fluxes are plotted as function of wavelength and fitted together with observations flux-points. In overall, our fitting produced statistically good fits for the majority of the set of the selected galaxy sample. We present our best fit model in order of good fit in Figure 3.1, 3.2, 3.3, 3.4, 3.5 where the numbers of good fits is approximately $\sim 60\%$.

Therefore, there are some poorly fit galaxies seen either in the optical or in the K-band infrared magnitudes presented in Figure 3.6 and 3.7. We explore several possibilities for these poor fits including defects in the photometry, imaging, library incompleteness, and the limits of the photometry.

First we inspected each object individual to verify the quality of the detection. We found no cosmic defects, any edge effects, or catastrophic failures in the photometry. Next, we compared the observed photometry to empirical spectra library that includes an active galactic nuclei (AGN) templates. We carry out a further fitting by making use of an on-line AGN spectra model from the SWIRE Template Library (Polletta et al., 2007). This publicly available template is originally generated from GRASIL code (Silva et al. 1998). It contains 25 templates including 3 ellipticals, 7 spirals, 6 starburst, 7 AGNs and 2 composite spectra of starburst+AGN templates covering the wavelength range between 1000 $\mathring{A}$ to 1000 micron; more details can be found at http://www.iasf-milano.inaf.it/.

In particular, we re-fit the two poorest fitted sources by Bruzual & Charlot (2003) and Conroy et al. (2009) library. We found that ID = 2045 has been picked up to be similar to a starburst SEDs template of IRAS 22491-1808 while ID = 777 is predicted to be QSO1; which is made up of spectra of composite quasar plus IR fluxes. However, we stress that these re-fitting have even worse $\chi^2_{\min}$ and are extremely unfit these objects. Overall, the AGN templates did not improve the quality of our objects best-fit. We thus reject the AGN templates in further analysis.

Finally, we verified the photometric catalog and the photometric errors for the sources. For two objects, we find that a potential reason why the K-band is somehow off is due to detection limit i.e an excess difference between the observed. We thus applied the upper limits as described in Section 2.6. For these data, the fits are relatively insensitive to the K-band due to its large errors.
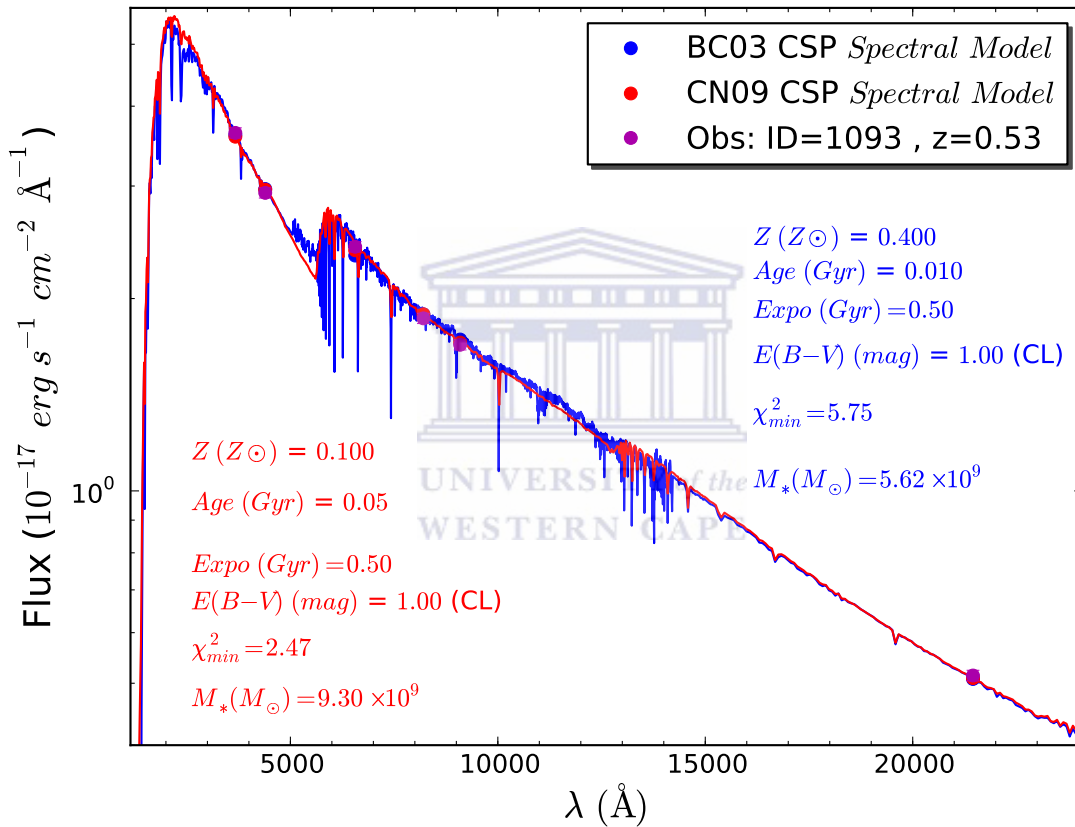
Figure 3.1: Figures show the best-fit model; the best fit parameters are printed upon each single plot. The SEDs model of Bruzual & Charlot (2003) are in blue while it is shown in red color for Conroy et al. (2009). The two model spectra are plotted together with the observed data in purple.
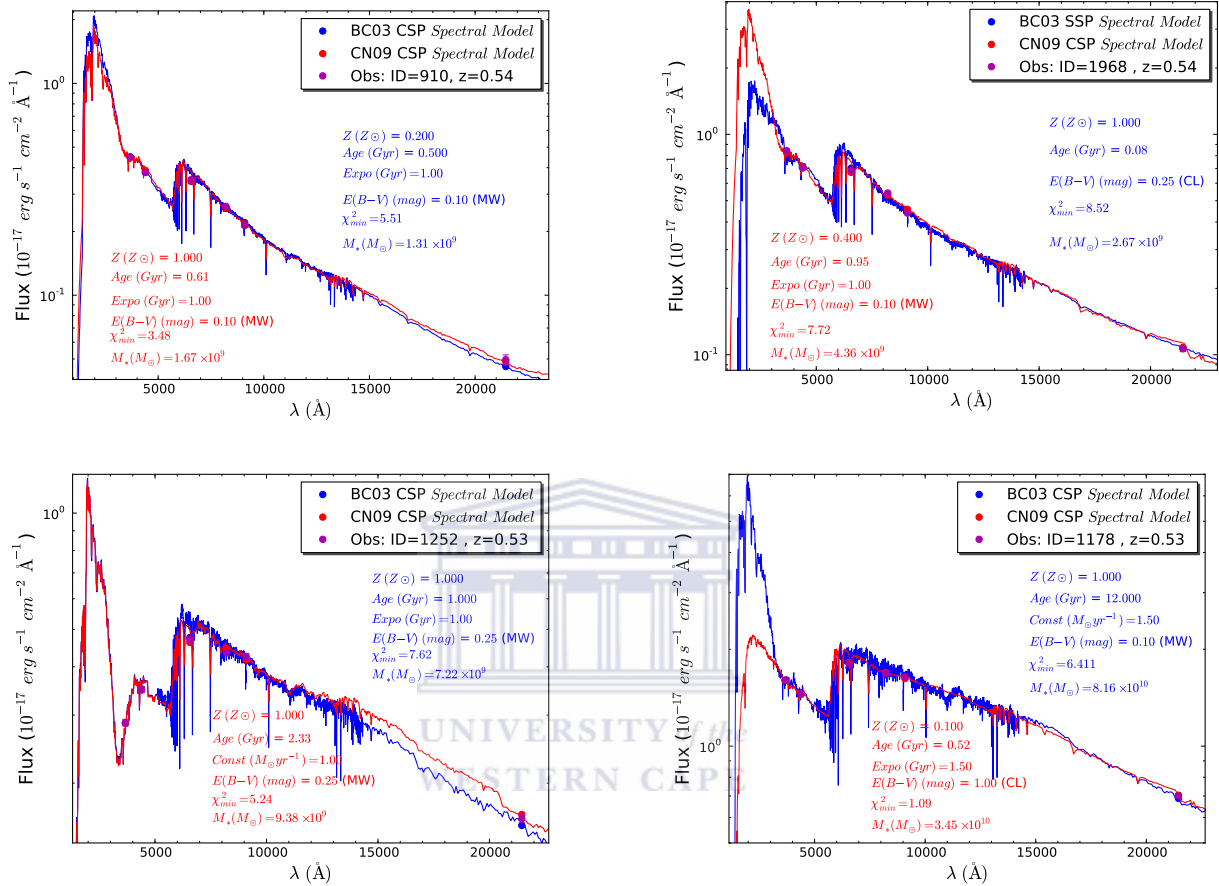
Figure 3.2: Good fits; the best fit parameters are printed upon each single plot. The SEDs model of Bruzual & Charlot (2003) are in blue while it is shown in red color for Conroy et al. (2009), and data point in purple.

3.6 Monte Carlo Error Analysis

Physical parameters derived from SED fitting are subject to substantial degeneracies and systematic uncertainties, mainly because of the difficulty in constraining the star formation history (Papovich et al. 2001). Given the well-known degeneracies between age and extinction in SED modeling, and other few non negligible propagation of uncertainties within the computed parameters range, we would like to know the effects on our mass measurements. We examine the effects of the assumed star formation history, and of photometric error that is particularly contributing uncertainty to the fluxes for each band (Dahlen et al. 2008). Thus we perform a substantial error analysis through a series of

Table 3.4: Results: derived Stellar Masses from GALAXEV (M_* in units of $10^9 M\odot$)

Obj	z	Best-fit	Min	Max	Std	Mean	$\frac{Std}{Mean}$
0	0.5315	1.173	0.925	1.344	0.107	1.175	0.091
1	0.5271	5.625	5.530	20.530	3.855	7.165	0.538
2	0.5321	22.739	11.996	39.134	5.980	22.218	0.269
3	0.5299	81.666	35.823	92.135	20.778	66.357	0.313
4	0.5388	7.221	7.096	9.359	0.722	7.897	0.091
5	0.5309	0.369	0.300	1.602	0.201	0.584	0.345
6	0.5677	3.099	2.450	4.543	0.604	3.491	0.173
7	0.5422	0.275	0.216	0.697	0.071	0.282	0.251
8	0.5285	8.020	1.612	8.516	2.728	4.705	0.579
9	0.5440	2.676	2.262	4.070	0.530	3.340	0.158
10	0.5133	0.642	0.213	0.722	0.137	0.552	0.249
11	0.5478	4.598	1.131	5.987	0.881	3.977	0.221
12	0.5297	3.619	3.293	7.130	0.656	4.076	0.161
13	0.5347	0.641	0.570	1.154	0.118	0.652	0.182
14	0.5258	4.406	2.397	9.376	2.037	5.497	0.370
15	0.5454	0.169	0.154	0.488	0.090	0.233	0.387
16	0.5417	0.443	0.379	0.484	0.021	0.430	0.048
17	0.5366	4.581	2.592	6.429	0.863	4.753	0.181
18	0.5381	3.527	2.752	5.476	0.799	3.677	0.217
19	0.5512	12.397	9.092	20.981	2.877	12.810	0.224
20	0.5381	0.194	0.157	0.216	0.014	0.186	0.074
21	0.5482	1.116	0.324	1.992	0.368	1.096	0.336
22	0.5401	1.312	0.873	3.046	0.292	1.230	0.237
23	0.5313	2.292	0.322	2.873	0.480	1.945	0.246
24	0.5319	0.668	0.578	1.117	0.097	0.685	0.142

Table 3.5: Table of the derived Stellar Masses from FSPS (M_* in units of $10^9 M\odot$)

Obj	z	Best-fit	Min	Max	Std	Mean	$\frac{Std}{Mean}$
0	0.5315	1.004	0.905	1.732	0.267	1.143	0.233
1	0.5271	9.300	4.246	17.336	2.068	8.876	0.233
2	0.5321	40.438	13.231	43.786	12.011	30.083	0.399
3	0.5299	34.523	15.313	54.390	4.817	30.862	0.156
4	0.5388	9.382	7.874	10.995	0.677	9.261	0.073
5	0.5309	0.399	0.366	1.160	0.174	0.606	0.287
6	0.5677	3.239	2.878	5.723	0.635	3.585	0.177
7	0.5422	0.235	0.054	0.563	0.136	0.224	0.606
8	0.5285	1.841	1.688	4.652	1.000	2.827	0.353
9	0.5440	4.367	3.155	6.820	0.575	4.180	0.137
10	0.5133	0.516	0.041	0.690	0.201	0.361	0.55
11	0.5478	5.380	2.166	5.650	0.977	4.942	0.197
12	0.5297	8.175	4.750	8.520	1.480	6.966	0.212
13	0.5347	0.625	0.556	0.677	0.012	0.624	0.019
14	0.5258	10.058	8.740	12.747	0.582	9.841	0.059
15	0.5454	0.168	0.149	0.392	0.056	0.203	0.276
16	0.5417	0.386	0.348	0.675	0.129	0.478	0.271
17	0.5366	6.047	1.984	6.222	0.557	5.831	0.095
18	0.5381	4.831	4.409	7.423	0.658	4.896	0.134
19	0.5512	1.948	8.488	21.812	4.084	14.013	0.291
20	0.5381	0.163	0.034	0.258	0.050	0.154	0.322
21	0.5482	1.198	0.593	1.950	0.239	1.088	0.220
22	0.5401	1.676	0.965	2.510	0.347	1.529	0.227
23	0.5313	1.668	0.106	2.085	0.499	1.119	0.446
24	0.5319	7.471	0.159	1.028	0.103	0.784	0.132
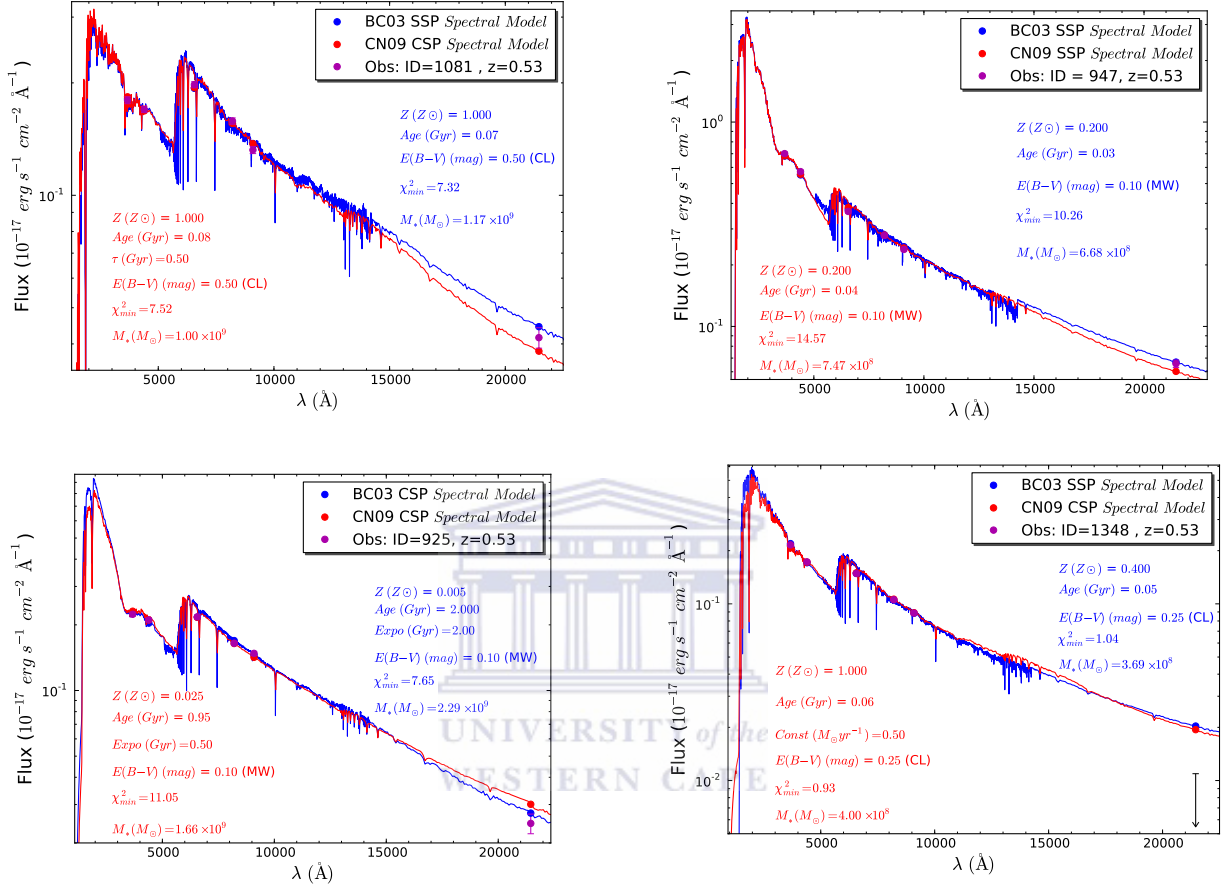
Figure 3.3: Figures show the best-fit model; best fit parameters are displayed. The SED models of Bruzual & Charlot (2003) and Conroy et al. (2009) models fit the observed spectra well as they are shown together with our data.

Monte Carlo simulations to estimate uncertainties on the derived masses. The method perturb the colors of each galaxy according to its photometric error, and determine the best-fit model for the perturbed colors. We conduct over one hundred and fifty trials for each galaxy, and generate lists of the best-fit mass. The generated minimum, maximum, standard deviation (std), mean mass, and the ratio of std and mean mass from simulations are gathered in Table 3.4 and 3.5 and utilized for error bar estimates. The calculated average error in the stellar mass measurement from GALAXEV and FSPS amount to ~ 0.218 and 0.141 dex (in Log(M_*)), respectively which is in good agreement with the estimated error of Brinchmann & Ellis (2000); (0.2 dex; in Log(M_*)).
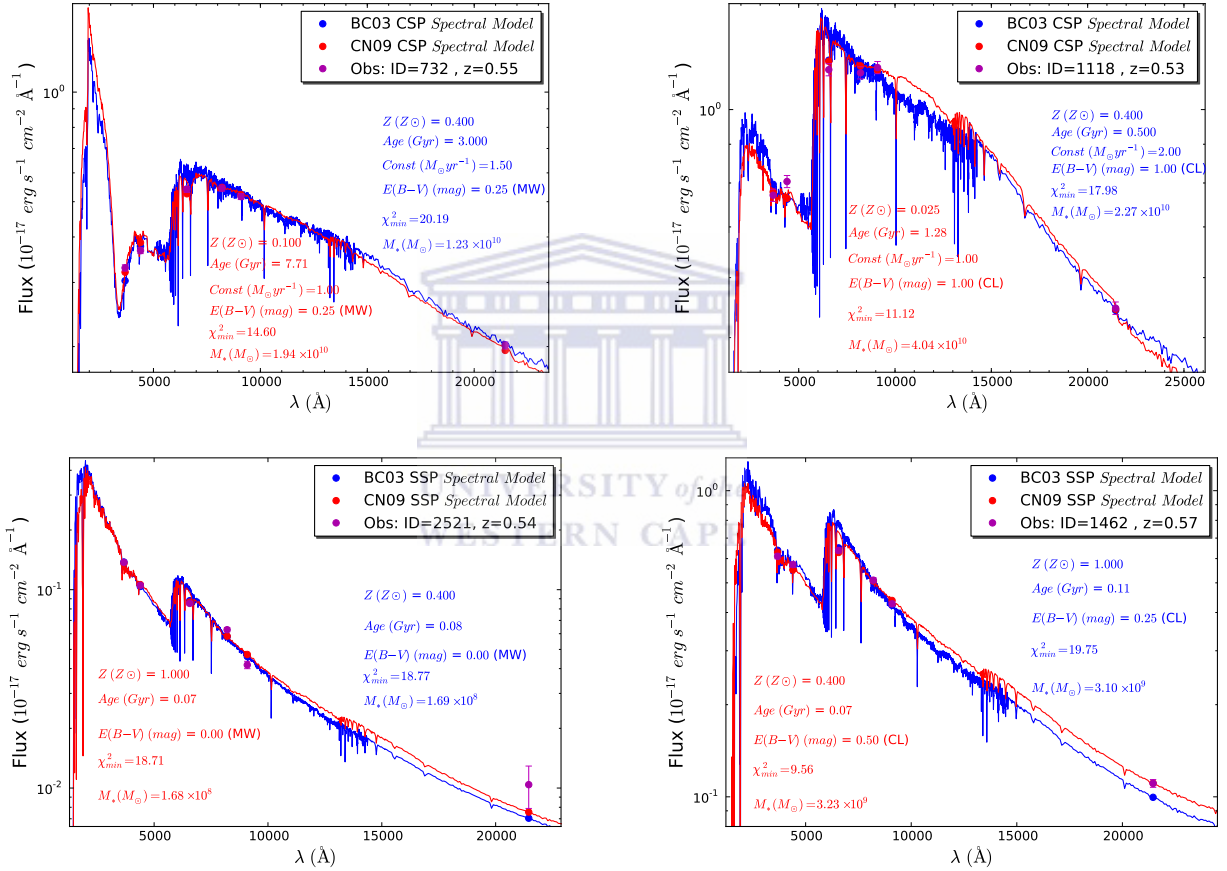
Figure 3.4: The SED model from Bruzual & Charlot (2003) and Conroy et al. (2009) fit the observed spectra well. They are plotted together with our data, informations of the best fit parameters are shown as well.
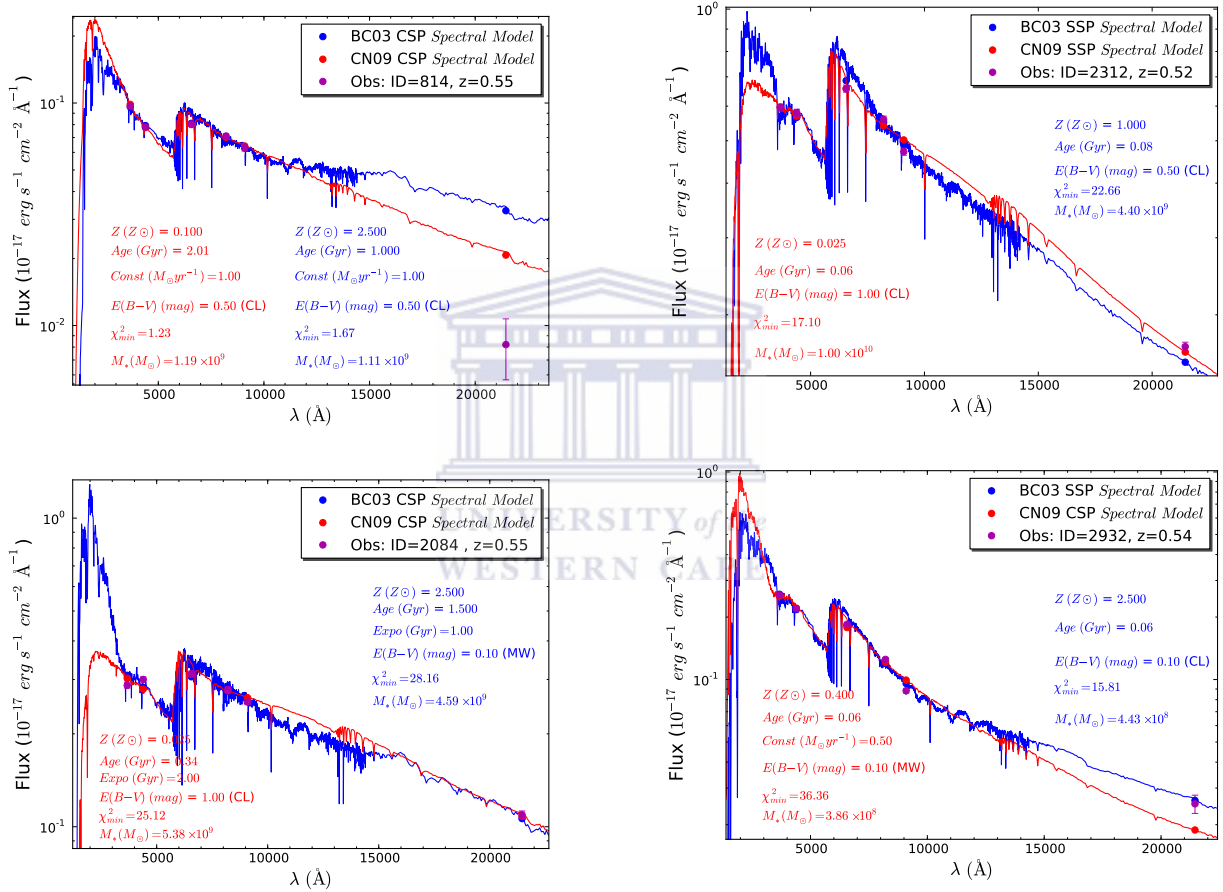
Figure 3.5: The K-band luminosity and photometry are under and over-fitted; the observed spectra in K passband is off compared to model SEDs of Bruzual & Charlot (2003) and Conroy et al. (2009) models. They are plotted together with our data; best fit parameters are all shown upon each plot.
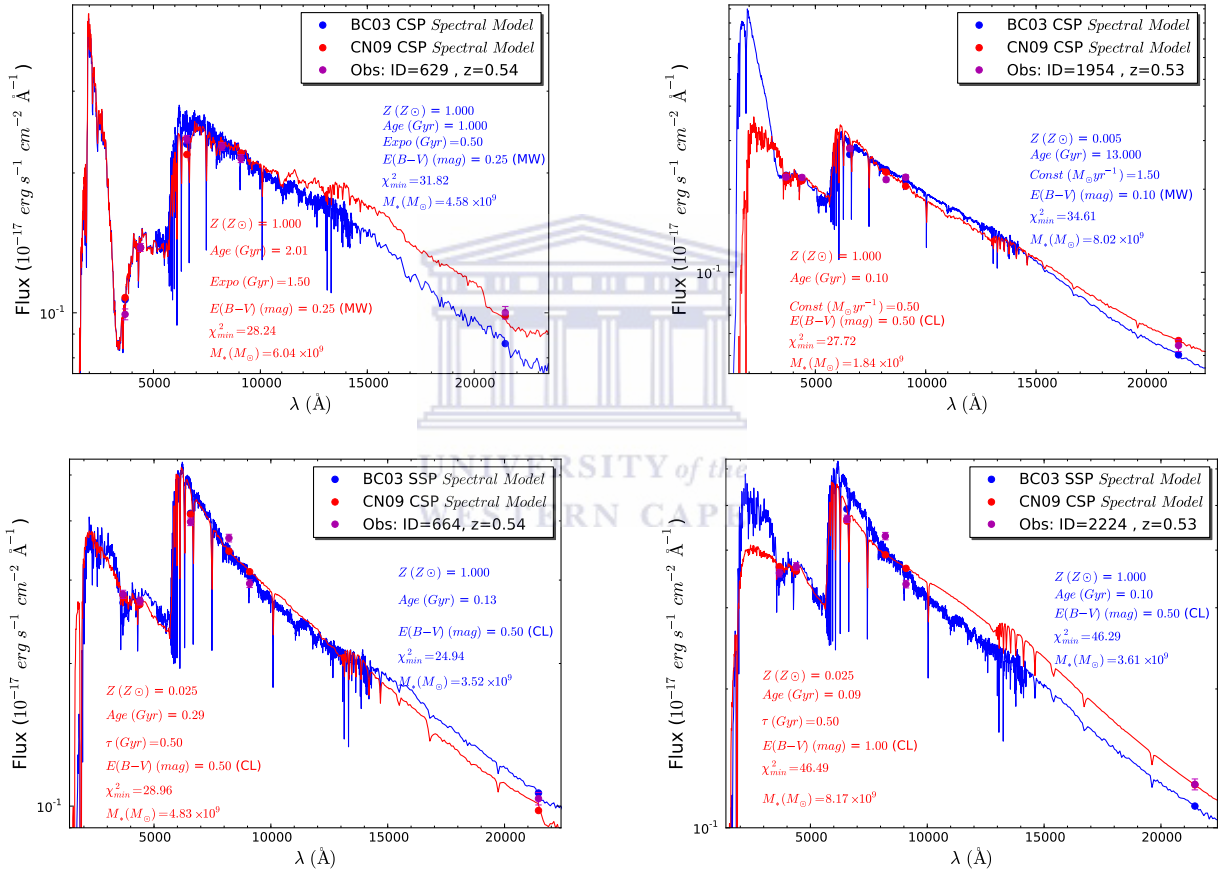
Figure 3.6: Poor fit, the best fit parameters are shown. SEDs from Bruzual & Charlot (2003) and Conroy et al. (2009) models are plotted together with our data.
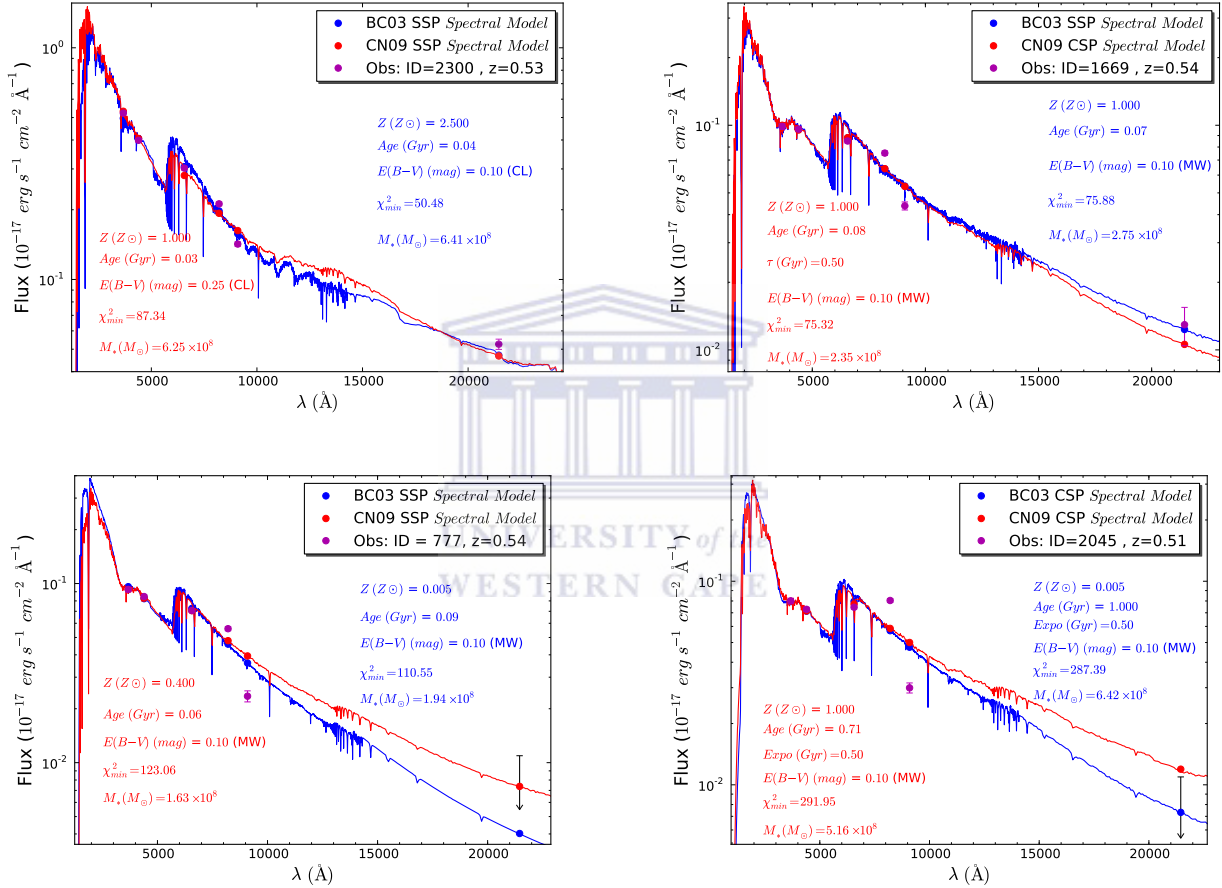
Figure 3.7: The observed point fluxes are off compared to spectra from Bruzual & Charlot (2003) and Conroy et al. (2009) models, poorly fit. The K-band flux point has been corrected by plotting the upper limit; see Subsection 2.6, however $\chi^2_{\min}$ has not been re-calculated. Thus robust interpretation of $\chi^2_{\min}$ will be disregarded in the main analysis as the fitting of the six filters involved have been untouched after correction.

Chapter 4

Stellar Masses

In recent years, some of the physical processes driving galaxy evolution have been implemented in numerical and semi-analytic models, including mass-dependent star formation (Menci et al. 2005; Bundy et al. 2006). It is useful to explicitly determine the physical properties of galaxies to further understand the physical processes and the evolution seen in galaxy clusters and the field. In particular, the stellar mass estimate is useful because it is not affected by morphological transformation or mergers i.e no bias either against galaxy type or orientation (Brinchmann & Ellis 2000). Stellar mass determination provides a snapshot of the star formation history and helps for understanding the baryonic mass of a galaxy.

As first shown by Brinchmann and Ellis (2000), stellar mass can also be a powerful tracer of galaxy formation. The most common method for measuring the stellar mass is to fit broad-band galaxy photometry to synthetic spectral energy distributions (SEDs). In this thesis, we present an implementation of this method and discuss the measurement of the stellar mass for star forming galaxies at intermediate redshift. We have deep WIYN 3.5m observations in UBRIz and two narrow band filters along with Palomar 5m K-band observations available from a public archive (Moran et al 2007). Measurements of the stellar mass will require fitting of observed photometry to SEDs model; see Section 3.4.

In Section 4.1, we provide a summary of the stellar mass estimates of our galaxy sample along with a discussion of the results. In Section 4.2, we carry out comparisons of the derived stellar masses from both SPS models. Finally, in Section 4.3 and Section 4.4, we further discuss our findings that include comparison of models and stellar masses to galaxy properties.

4.1 Stellar Mass Estimates

We have described thoroughly our stellar mass estimator in Chapter 3. However, we highlight some of the key points here. In this work, stellar masses are determined by fitting model SEDs to UBRIzK photometry. We compare the observed SED of 25 spectroscopically confirmed star forming galaxies with two large libraries of SED models and obtain the stellar masses from the normalization of the best-fit model to the data.

The observed SED of each galaxy is compared to a grid of 28800 models from Bruzual & Charlot (2003) and 47520 from Conroy et al. (2009) that span a wide range of metallicity, ages, star formation histories (parametrized as an exponential, burst and constant) and dust content. Most of the assigned star formation histories provide adequate fits to the objects. Uncertainty propagation in the fitting are determined from a large number of (one hundred and fifty) trials through Monte Carlo simulations in which the input photometry is varied according to the photometry errors. Finally, in Table 3.3, we report a summary of the best fitting parameters values that include ages, metallicity and amount of dust.

4.2 Comparison of Models

We carried out a comparison of the two SPS models and its robustness for measuring masses of star forming galaxies. The Bruzual & Charlot (2003) SPS is designed to provide spectra at high resolution of 3 Å with a mass range of 1-100 $M_\odot$ at an interval age of 1-14 Gyr. While the Conroy et al. (2009) SPS does not have such resolution but is recently claimed to have handled in a more advanced way, all the different systematic uncertainties such as the one from stellar evolution prescription and dust treatment (TP-AGB evolutionary phase implemented using isochrone synthesis). Nevertheless, for a very narrow error range as estimated in Section 3.6, the average stellar masses derived from the two models are in excellent agreement. Figure 4.1 shows directly that the correlation between the derived stellar masses is quite tight. For lower mass galaxies, however, there is trend that Conroy et al. (2009) may have significant uncertainties as compared to Bruzual & Charlot (2003).

We fit the derived stellar mass from GALAXEV versus FSPS with linear least square of slope $\simeq 1.008$ and intercept $\simeq$ -0.044. The one-to-one line (equal mass) is plotted in Figure 4.1, and from which one can show directly that the two calculated masses are well correlated. Furthermore, within the range of estimated error bars, it can be seen that both calculated masses are in excellent agreement.
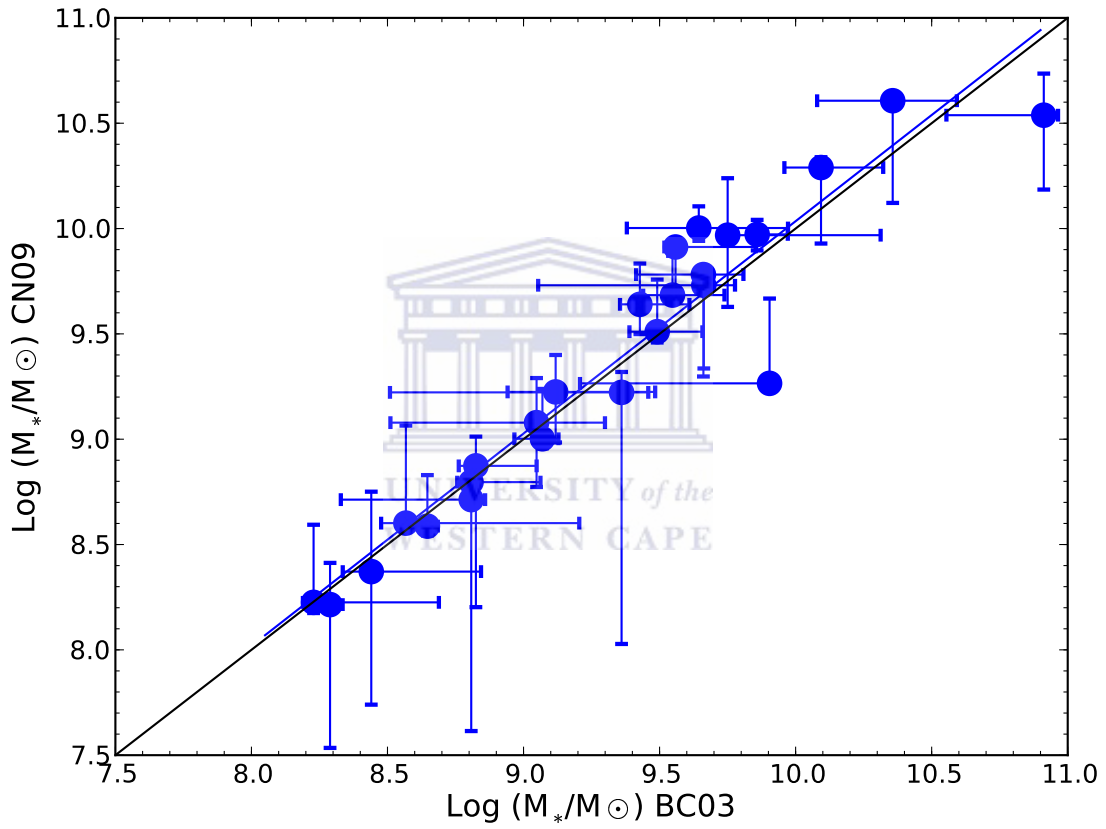
Figure 4.1: Comparison of stellar masses derived from GALAXEV and FSPS at different metallicity and SFR history. The best fit straight line from least square method and the one-to-one line are plotted. The asymmetric error bars represent the minimum and maximum mean stellar mass that were estimated using Monte Carlo simulation.

4.3 Comparing the Models with galaxy properties

Here we further compare the two models with respect to galaxy properties. We derived the ratio of masses between the two models with respect to the magnitude, color, and mass of our sample.

The two models behave similarly with respect to galaxy properties where the enhancement of faint galaxies dominates in Bruzual & Charlot (2003). As seen in Figure 4.2, galaxies with faint R magnitudes tend to have higher masses as measured using the models from Bruzual & Charlot (2003) while FSPS models result in measuring higher mass for bright galaxies. The two models predict the same mass around R=22.

The color versus the stellar mass ratio of our sample is shown in Figure 4.3 . It shows the Conroy et al. (2009) models result in higher masses for redder galaxies. Figure 4.4 compares the models as a function of stellar masses. At stellar masses less than $10^{9.0}$ $M_\odot$, both mass estimates are in good agreement. For stellar masses greater than that, the GALAXEV models produce lower masses than FSPS.
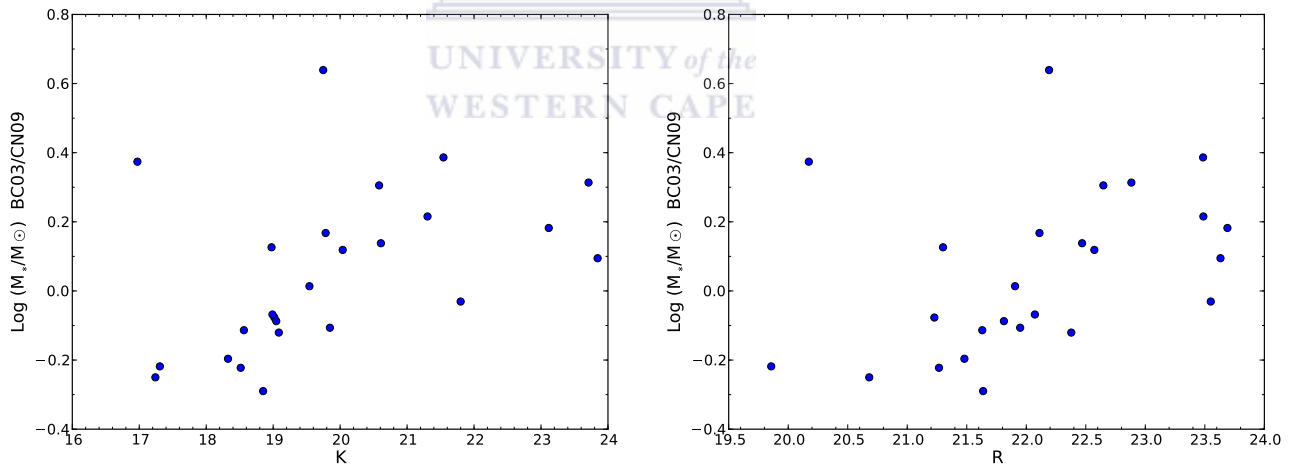
Figure 4.2: (Left): K-Band magnitude vs. Stellar mass ratio. (Right): R-Band magnitude vs. Stellar mass ratio.
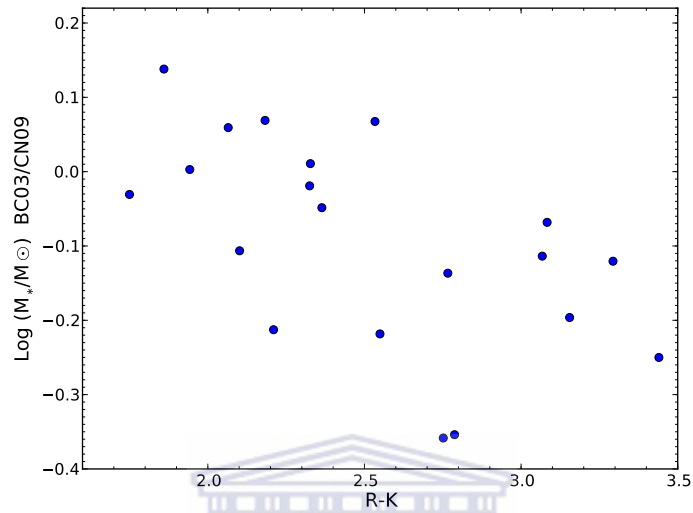
Figure 4.3: (R-K) color vs Stellar mass ratio
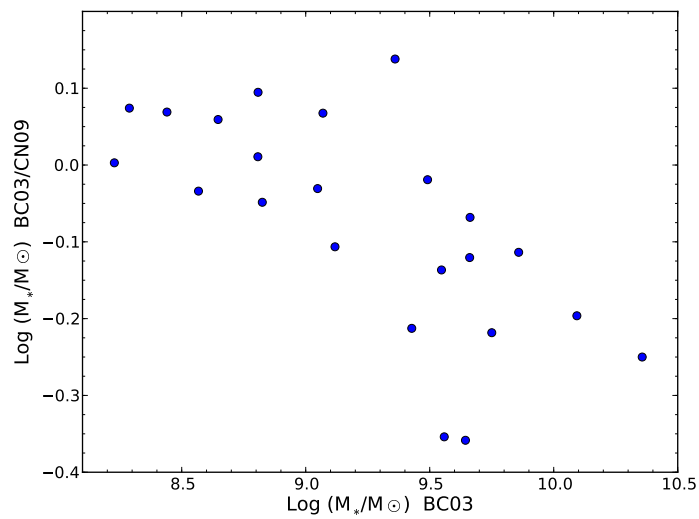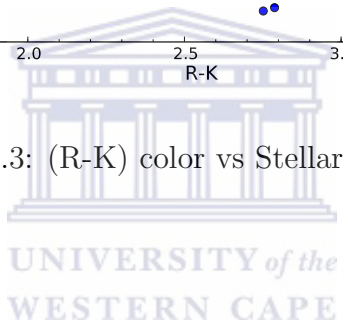
Figure 4.4: Plot of stellar mass estimated from Bruzual & Charlot (2003) vs. stellar mass ratio

4.4 Stellar Mass to galaxy properties

Here we compare the stellar mass to the properties of the galaxies. From the magnitude versus stellar mass diagram in Figure 4.5, the most distinct trend seen here is that massive galaxies tend to be luminous, and faint galaxies are lower mass. Figure 4.6 shows that the massive galaxies tend to be redder in our sample. These trends are quite significant with regards to the big picture of galaxy evolution study where massive galaxies are found to be red, old and quiescent while lower mass galaxies are blue, young and still undergoing a star formation activity.
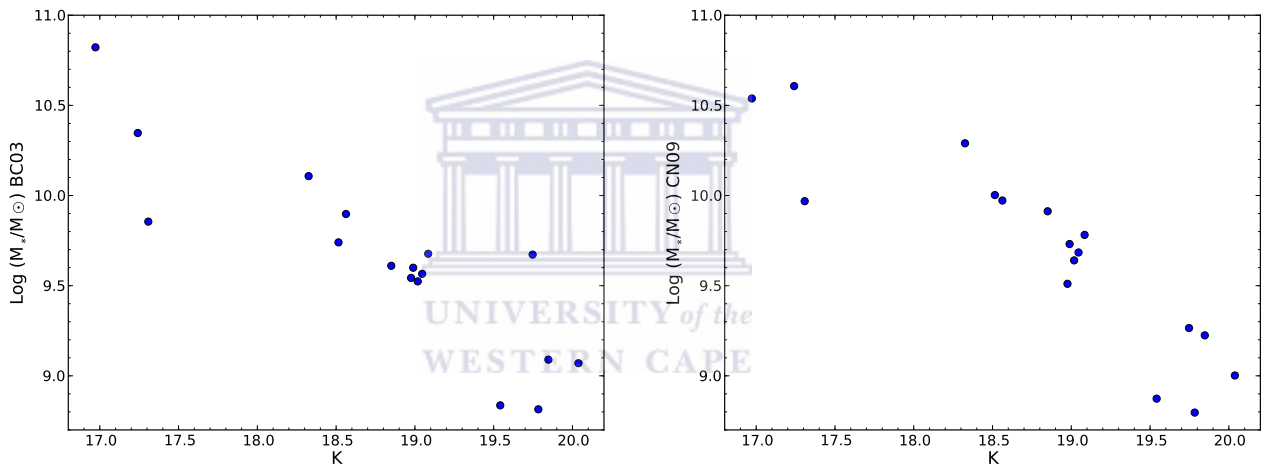
Figure 4.5: (Left): K-band vs. Stellar mass of Bruzual & Charlot (2003). (Right): K-band vs. Stellar mass fo Conroy et al. (2009)
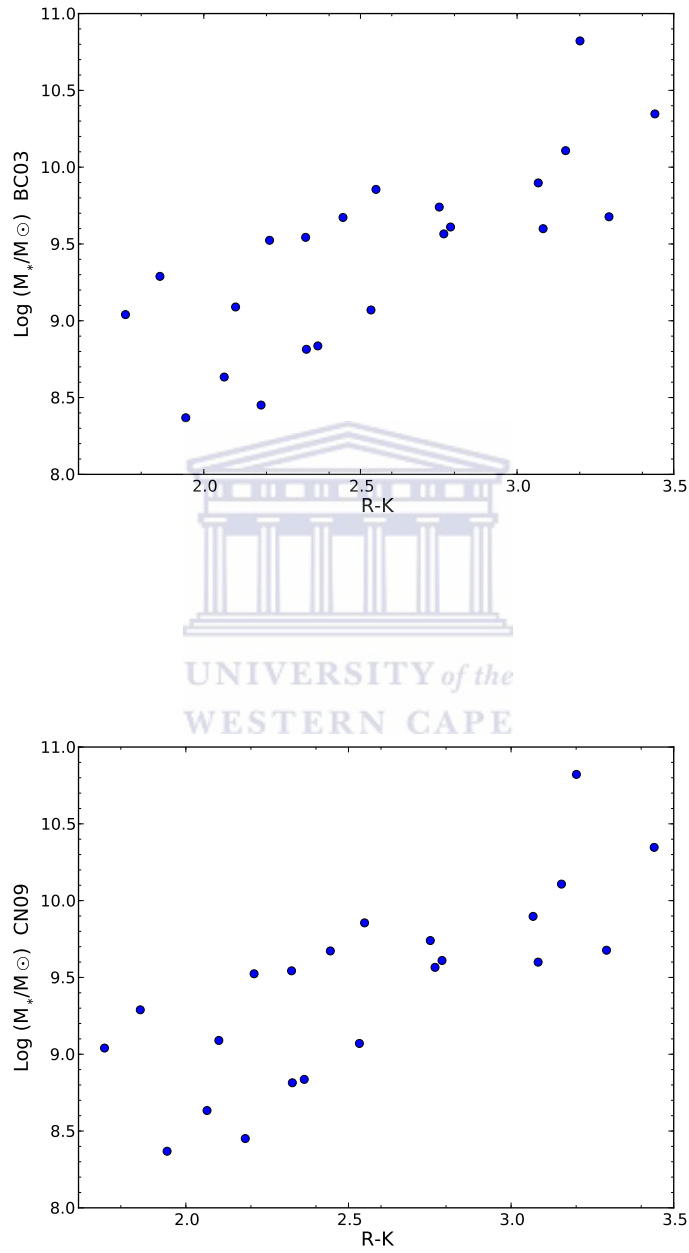
Figure 4.6: (Top): (R - K) color vs. Stellar mass of Bruzual & Charlot (2003). (Bottom): (R - K) color vs. Stellar mass fo Conroy et al. (2009).

Chapter 5

Results

Section 5.1 deals with a detailed procedure for dynamical mass measurements and presents other galaxy properties as reported in Table 5.1. In Section 5.2, we compare our derived stellar and dynamical masses, and we compare our results to previous work performed by Guzmán et al. (2003) that examines a sample of field galaxies. Finally, Section 5.3 provides an in depth analysis of the results followed by an extensive discussion. For comparison to Guzmán et al. (2003), we use the stellar masses derived using the (Bruzual & Charlot, 2003) model.

5.1 Dynamical Mass

In this section, we provide a summary of spectroscopic measurements that will be presented in Crawford et al. (2011). The equivalent width and velocity dispersion were determined by fitting a single or double Gaussian functions to the line profile for each emission line object in the sample at [OII]λ3727, Hβ, and [OIII]λ5007. In our DEIMOS data, [OII]λ3727 was resolved into two components and it was fit with a double Gaussian. All fits were visually checked for quality. A small selection of the objects did have rotation curves that were visible in the 2D data, and for these objects, we measured the velocity centroid and dispersion as a function of spatial position along the slit.

We follow the procedure from Guzman et al. (1997) and subtract, in quadrature, the instrumental dispersion from the measured value to recover the velocity dispersion of the galaxy. For most sources, we estimated the instrumental dispersion based on measurements of nearby sky lines. For one mask (w05.m2), the seeing during the observations was exceptional and compact source did not fill the slit. Their velocity dispersion for all lines was well below the value measured for the sky lines in the spectra. For these sources, we estimate their seeing based on their spatial extent in the slit and correct the dispersion of the sky lines based on the sources not filling the slit. There may be other masks where this was a problem and so for our most compact sources, we may be underestimating the velocity dispersion. At worse case, this would introduce an uncertainty of approximately a factor of 2. Based on measurement errors of the data, we estimate that the smallest velocity dispersion that we can safely recover is 10 km s^{-1}. Any value below this is reported as an upper limit. After correcting for the instrumental effects, we
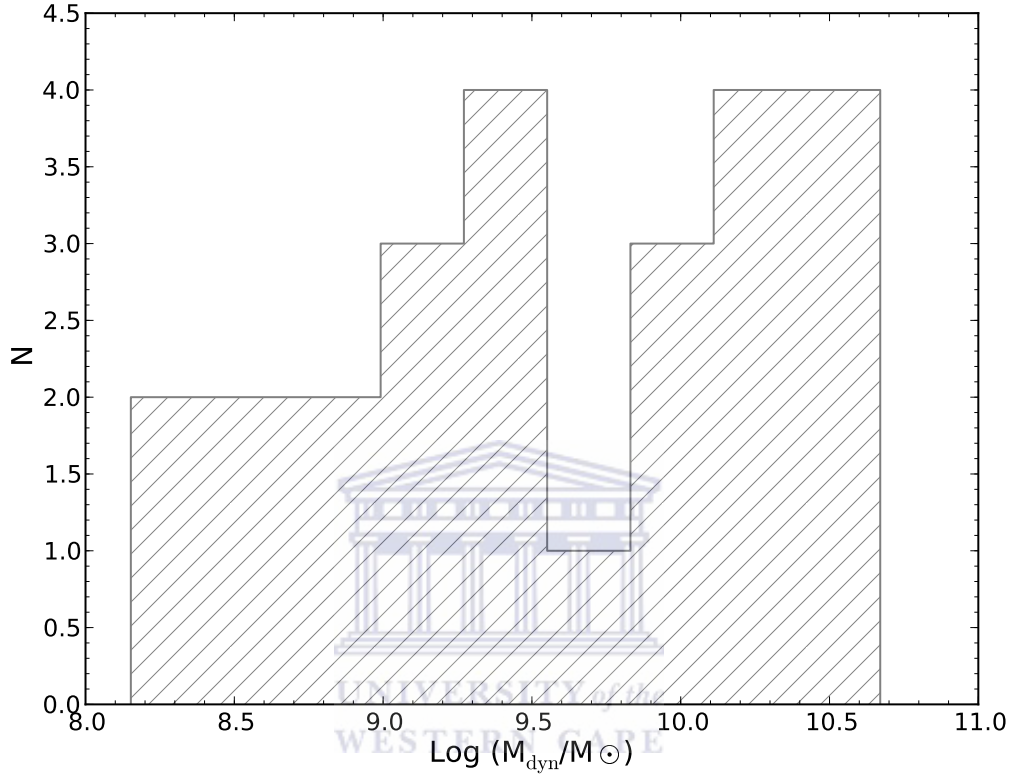
Figure 5.1: Distribution of the dynamical masses estimated from [OII]λ3727 emission lines

determine the final velocity width of each source by calculating the weighted average of the measurements for the three lines. The weights are based on the inverse variance for each of the lines. All observed velocity dispersion are corrected to the rest frame. The average velocity dispersion from all of the lines is reported in Table 5.1.

Using the average velocity width and best size measurement , we calculate the dynamical mass of teach system following Phillips et al. (1997) as:

$$M_{dyn} = \frac{3c_2\sigma_v^2 r_e}{G}$$

We adopt $c_2 = 1.6$. Following Guzman et al. (2003), we correct this velocity dispersion for a factor of 1.3 for using emission lines for the measurement. In Table 5.1, we provide the measured dynamical masses along with other rest frame properties of these sources.

Table 5.1: Measured parameters of the sample galaxies, M_{dyn} and recalculated re-M_{dyn} $(10^8 M_\odot)$ using the upper limits $(\sigma \leq 35$ km s$^{-1})$ respectively.

ID	I_{814}	σ (km/s)	r_e (arcsec)	R_e (kpc)	M_B	M_{dyn}	re-M_{dyn}
1081	22.0633	44.890	0.370	2.332	-19.090	68.17	52.50
1093	19.3855	19.460	1.099	6.946	-22.460	38.16	95.00
1118	19.9392	58.950	1.080	6.803	-21.610	342.99	264.00
1178	19.4946	49.400	1.063	6.705	-22.180	237.39	183.00
1252	20.964	63.580	0.375	2.352	-20.100	137.94	106.00
1348	22.5019	27.800	0.266	1.677	-18.760	18.80	22.90
1462	20.7912	67.780	0.661	4.070	-20.770	271.26	209.00
1669	22.8702	33.270	0.245	1.533	-18.100	24.62	21.00
1954	21.721	21.980	0.377	2.381	-19.520	16.69	32.60
1968	20.7264	30.110	0.290	1.812	-20.480	23.84	24.80
2045	22.7969	12.780	0.323	2.060	-17.590	4.88	28.20
2084	21.4483	48.130	0.498	3.105	-19.880	104.36	80.30
2224	20.9792	61.870	0.537	3.388	-19.830	188.14	145.00
2300	21.7445	21.430	0.282	1.773	-19.650	11.81	24.20
2312	20.6919	11.340	0.818	5.174	-20.780	9.65	70.80
2521	23.0649	19.760	0.199	1.243	-18.250	7.04	17.00
2932	22.3174	9.030	0.289	1.809	-19.170	2.14	24.70
629	21.6651	51.550	0.697	4.377	-19.700	168.76	130.00
664	21.146	42.320	1.581	9.920	-20.150	257.77	198.00
732	20.7201	76.900	0.877	5.457	-20.610	468.18	360.00
777	23.1908	7.450	0.281	1.763	-18.030	1.42	24.10
814	22.9313	10.890	0.255	1.590	-18.250	2.74	21.70
910	21.5125	21.850	0.237	1.485	-19.910	10.29	20.30
925	22.0194	21.420	0.471	2.968	-19.340	19.76	40.60
947	21.4468	46.940	0.439	2.766	-19.810	88.41	68.00

5.2 Comparison between Cluster and Field

5.2.1 Stellar and Dynamical Mass

We have come to a comparison of the galaxies' stellar and dynamical masses. In the local universe, significant correlation between stellar and dynamical mass of the form $M_{dyn} = M_*^\alpha$ has been observed (Padmanabhan et al. 2004; Bundy et al. 2007), however such correlation will exist only if the stellar mass makes up a relatively constant fraction of the dynamical mass over the full range of stellar masses. We search for relationship between stellar and dynamical mass and map galaxy evolution as function of environment. Bundy et al. (2007) find a value of $\alpha = 1.23 \pm 0.17$ where they adopt a zero-point $M_{dyn} \equiv M_*$ at $10^{11} M_\odot$ with typical uncertainty of ~ 0.2 dex. In Figure 5.2, we plot stellar mass vs. dynamical mass for 25 galaxies for which we have determined both masses. We calculated $\alpha = 0.97 \pm 0.01$ at zero-point around $10^{9.5} M_\odot$.

We have derived stellar masses that have median value of $\sim 2.68 \times 10^9 M_\odot$, and an average of $\sim 6.94 \times 10^9 M_\odot$. The lower and upper derived stellar masses are respectively $\sim 1.69 \times 10^8 M_\odot$, and $8.17 \times 10^{10} M_\odot$. Approximately 44% of the galaxies in the sample have larger M_*/M_{dyn}, and this is clearly an unphysical situation. We discuss possible explanation for the fact that $M_* > M_{dyn}$ for these lower mass galaxies in Section 5.3. It is also important to focus on the derived masses of the significant fraction of the objects i.e the remaining 56% of the sample for which we have larger M_{dyn}/M_* later. Overall, at higher dynamical masses $M_{dyn} \gtrsim 10^{9.5} M_\odot$, our stellar masses are lower. However, at $M_{dyn} \lesssim 10^{9.5} M_\odot$, a large dispersion is seen in the relationship between the two. Although, a correlation is seen between the dynamical and stellar mass for all galaxies.
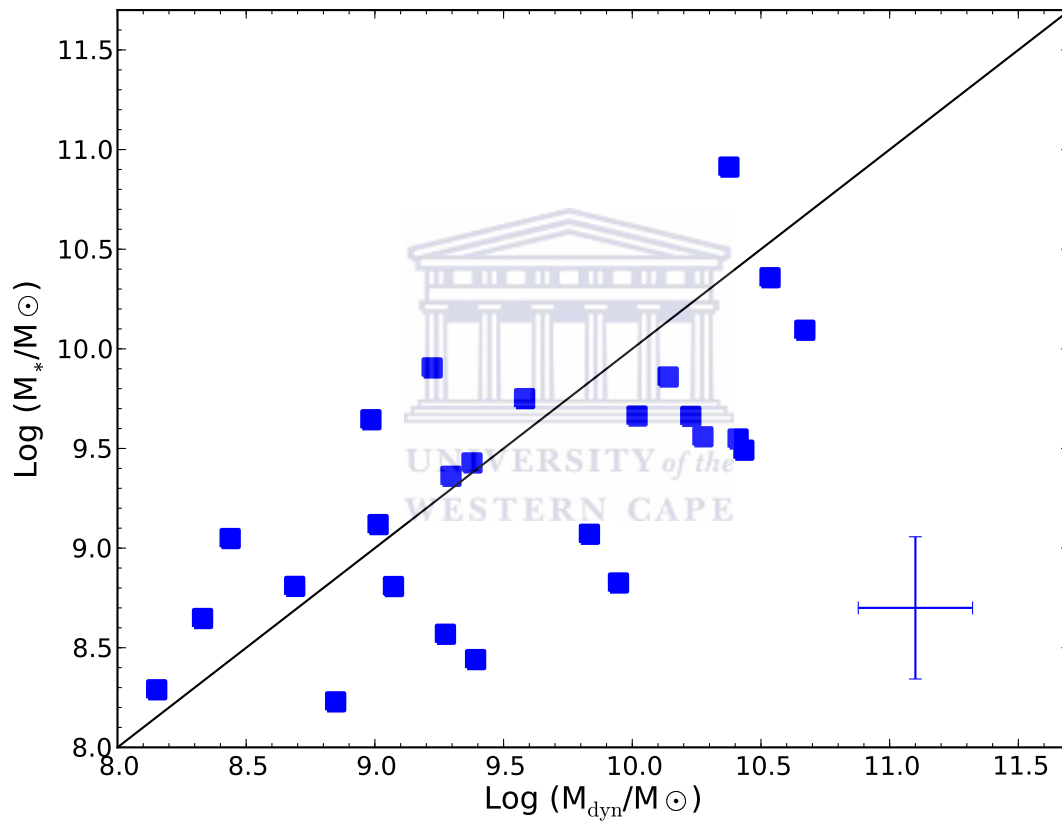
Figure 5.2: Stellar mass vs. dynamical mass for the entire sample of 25 galaxies at $z \sim$ 0.54. The one-to-one line is represented by black solid line. The points situated above the one-to-one line tend to have big χ^2.

5.2.2 Comparison with Guzmán et al.

We compare our results to those field galaxies studied by Guzmán et al. (2003). Their sample was originally composed of compact galaxies ($0.4 \lesssim z \lesssim 1$) from Phillips et al. (1997). Their selection criteria for compact galaxies were: half-light radius $r_{1/2} \leq 0.5$" with magnitude $I_{814} \leq 23.74$ and surface brightness $\mu_{I_{814}} < 22.2$ mag arcsec^{-2}. Since our galaxy sample was drawn from different observations, we have taken into account the selection requirements of Phillips et al. (1997) prior to comparing the two samples. We have culled our sample to have the same selection as Phillips et al. (1997). For conformity to the field sample, an upper limit ($\sigma = 35$ km s^{-1}) was applied for galaxies that have lower velocity dispersion in our sample.

The field sample from Guzmán et al. shows very similar behavior between stellar mass and dynamical mass and also displays the very low stellar to baryonic mass ratios. At $M_{dyn} < 10^{9.5}$ M$\odot$, there are some objects which Guzman et al. did not detect in their sample. These lower mass galaxies are faint objects and the small dynamical masses observed for these galaxies has been seen previously for cluster star forming galaxies (Koo et al. 1997) and imply these galaxies may evolve into the large population of low mass spheroidal galaxies seen in clusters today. These low mass galaxies were not present in the field sample of Guzmán et al. even though they could have been detected. However, massive galaxies exhibit similar behavior to objects in the field at the same redshift and apart from that our sample extends to low mass regimes that is not present in the field sample.
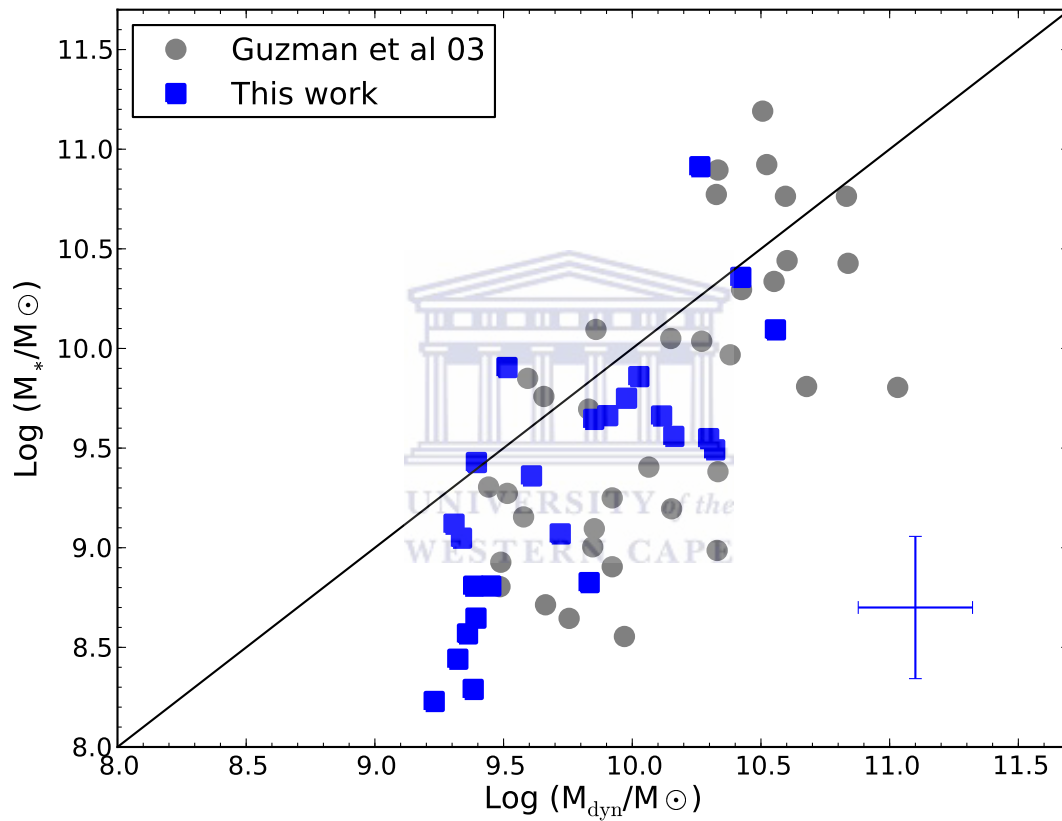
Figure 5.3: Stellar mass vs. dynamical mass. The one-to-one line is represented by black solid line. The square points in blue and gray show our sample and Guzman et al., respectively. These galaxies are selected on both the basis of compactness of Phillips et al. (1997) ($r_{1/2} \leq 0.5$") and using an upper limits ($\sigma \leq 35$ km s^{-1}) of those objects having a smaller velocity dispersion.
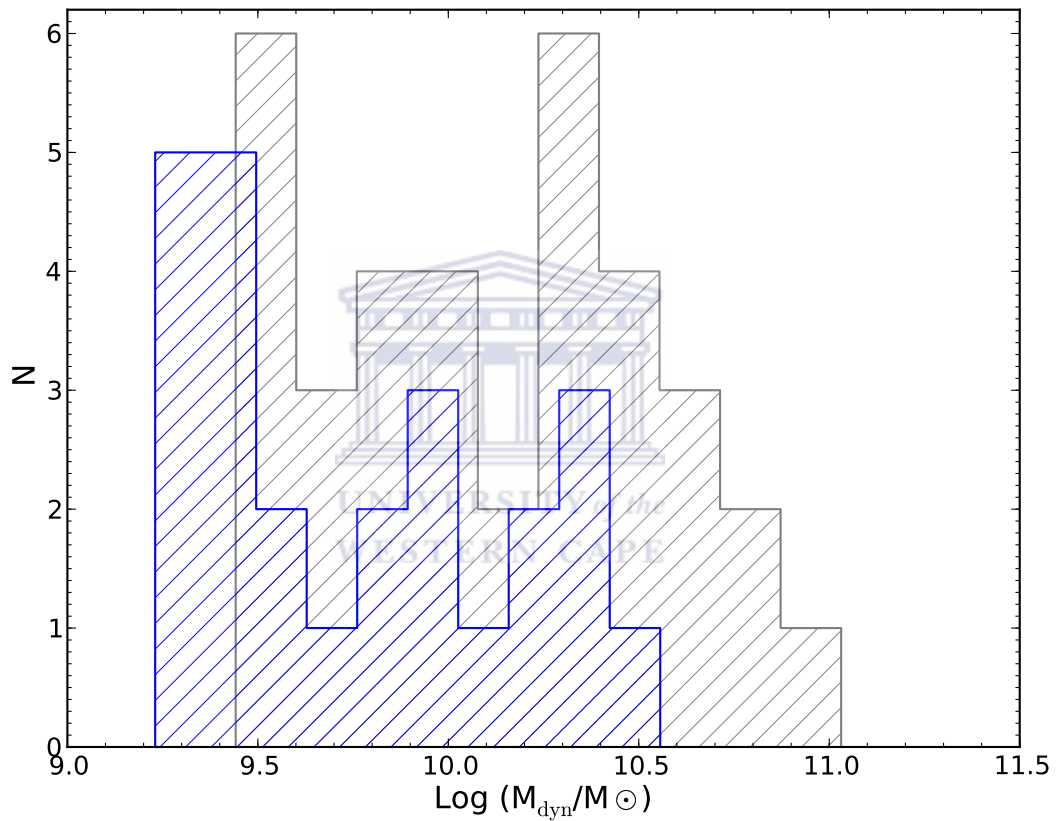
Figure 5.4: Distribution of (recalculated M_{dyn}) dynamical masses; color gray represents masses from Guzmán et al. and blue for this work. The galaxies are selected on both the basis of compactness of Phillips et al. (1997) ($r_{1/2} \leq 0.5$") and using an upper limits ($\sigma \leq 35$ km s^{-1}) of those objects having a smaller velocity dispersion. The color gray represents masses from Guzmán et al. and blue for this work.

5.3 Discussion

5.3.1 What explains $M_* \gtrsim M_{\mathrm{dyn}}$

We explore different explanations for the derived stellar masses that are found to be slightly higher than the dynamical masses. As can be seen from Figure 5.2 a number of sources have higher stellar mass, and this excess in mass is seen predominately at lower dynamical mass $M_{\mathrm{dyn}} \lesssim 10^{9.5}$. For an object in dynamical equilibrium, the dynamical mass should be greater or equal to the stellar mass and thus this is an unphysical situation.

First, we start by investigating the consistency of the estimated error bars. We plot one sigma error bar in Figure 5.2 where it is reasonable representation to our error analysis. Assuming that $M_{\mathrm{dyn}} \approx M_*$ for all objects, within the plotted error bars, we would expect relatively few objects above the equal-line, and these remaining objects might be due to scatter in the measurements.

Second, with regards to the derived stellar masses, in fact several possibilities may exist for having measured a stellar mass that is too high that are discussed in the rest of this section. We have reported that double-checking on the UBRIzK photometry and photometric error was performed, and the upper limit as described in Section 2.6 was applied. We found no obvious reasons that the photometry of any of these sources would bias the results.

We now discuss the SED fitting results by looking closely at the best χ^2 values. For some objects these chi-square seem to have huge values as shown by the figures in Section 3.5. This might be due to the factors discussed below such as an inappropriate star formation history in the SED template, incompleteness of SED library, or issues with the stellar evolution model.

Furthermore, the models contribute some degree of uncertainties to the derived physical properties. The systematic uncertainties from TP-AGB phase plus other uncertainties in the stellar evolution prescription should be accounted by caution (Conroy et al. 2009, 2010). The effect of metallicity and dust extinction (Garn & Best 2010) and the chosen IMF heavily affect the fitting results. A significant issue is library incompleteness and we may not fully cover the wide range of parameters in SFH, metallicity and IMF. However, even if one has templates with precise and accurate star formation histories, it may also suffer from the assumptions that go into them. Thus the reliability of one model is relative because comparisons between different models made by different authors using the same input parameters do not always give the same results (Drory et al. 2004).

Alternatively, we could bolster our library completeness through the multi-component

models to which can fit the observed SED with the superposition of two or more star formation histories, i.e both young burst and old population to estimate the stellar mass.

Next, there are large uncertainties in the measured dynamical mass. One of the major fact would be from some sources that are very close to the resolution limit. However, an investigation of whether these galaxies are rotationally supported and/or not in dynamical equilibrium should also be considered.

Finally, are these implying a lack of dark matter?. Our results suggests that these galaxies have relatively small amount of dark matter content, if any, (Covone & Napolitan 2004) but a theoretical justification for a lack of dark matter has not been shown. This conflicts with galaxy formation and evolution theories, and the presence of the dark matter seen in cluster probed by the X-ray and the weak lensing method. Nonetheless, this is an open question to be debated, and it motivates further study of these objects.

5.3.2   Differences between field and cluster sample

There has long been known that the local environment plays a very important role in galaxy evolution (Sato & Martin 2006) and thus it could be argued that the differences seen between the two samples in Section 5.2.2 could be real. We now discuss the different distributions of masses seen between the field and cluster samples. In particular, we consider and investigate few major points with regard to the origin of these lower mass galaxies in cluster. We thus provide suggestions that might give rise to the large differences between cluster and field masses. We discuss the possibility of infalling objects, in situ situation, and finally the effect of downsizing.

Are they an infalling population?

The difference seen between velocity distribution in different galaxy types (early-type component is serialized while late-type component is following a Gaussian distribution) has provided evidence that late-type galaxies are falling into clusters (Boselli & Gavazzi 2006). Assuming that the infalling processes had recently happened, the members of cluster sample should look like normal field star forming galaxies at some time in the past.

Thus if these galaxies fall onto the cluster for the first time, a simple scenario could globally be described as the following.

- As they fall onto the cluster they will undergo processes that will increase their star formation and strip materials. These various processes are including the gravitational interactions; eg: high speed galaxy-galaxy encounters within cluster, that

are expected to trigger star formation while at some point the interaction with the hot and dense intergalactic medium (IGM) will suppress the ongoing star formation activity due to gas depletion (Boselli & Gavazzi 2006).

- The in-fall time scale would depend on the position and velocity of the galaxy along with the mass of the cluster. As they are recently acquired through in-fall from the field onto the clusters. During some period $\triangle t$, they will have lost mass to end up being at the lower mass.

Are they found in situ?

It is also possible that these galaxies were formed in the cluster where they are just young newly formed galaxies. The lack of evidence for dominant older stellar populations found in our SED fitting results, see Table 3.3, would supports this idea.

Are they consistent with downsizing observation?

The halo mass plays a significant role in evolution that is described as downsizing (Cowie et al. 1996; Treu et al. 2005). In short, the principle of downsizing says that massive halos have formed their stars in the past within a relatively short period of time, while low mass galaxies are recently forming stars over a longer duration. From the age stellar mass relation, it has been found that low-mass galaxies have young stellar populations while more massive galaxies have significant amount of older stellar populations (Vergani et al. 2008), thus consistent with the downsizing observation.

Chapter **6**

Conclusions

6.1 Conclusion

The major aim of this work is to estimate and compare the stellar mass to the dynamical mass of star forming galaxies in intermediate redshift galaxy clusters and the field. We have presented the stellar mass estimates of an X-ray luminous cluster MS 0451.6-0305 at intermediate redshift from SEDs fitting technique. The SED model libraries are computed from GALAXEV and FSPS stellar population synthesis code of Bruzual & Charlot (2003) and Conroy et al. (2009) respectively that span a wide range of age, SFR history and metallicity. We have performed SEDs fitting through a standard χ^2 minimization technique: the observed SED of a given galaxy is compared and normalized to a set of template spectra. Note that we redshift-ed all model spectra to the redshift of each of our objects and referred all magnitudes to the Vega magnitude system.

We have discussed the fitting results in terms of uncertainty and model differences. We described the different effects of metallicity, SFH, age, and dust with respect to the spectra fit. We investigated the fits seen for a few galaxies and refined the fitting parameters by running extra analysis on empirical SEDs library to further test our findings. We performed a substantial error analysis on the measured stellar masses via Monte Carlo simulation. The best-fitting models were used to estimate the stellar masses. We compared the Bruzual & Charlot (2003) and Conroy et al. (2009) models and found reasonable agreement.

The major points that can be drawn from our results is that stellar mass estimates are fairly consistent with the dynamical estimates. In our sample, massive objects exhibit very similar behavior to objects in the field of Guzmán et al. (2003) while lower mass objects display higher dynamical mass to baryonic ratio. We have compared the derived stellar mass to the estimated dynamical mass and have found a strong correlation, however, our sample includes low mass objects which are not in the Guzmán sample.

6.2 Future Work

6.2.1 Expansion to other clusters

We have investigated the stellar populations of samples of star-forming galaxies at intermediate redshift in galaxy cluster MS 0451.6-0305. The physical properties including stellar and dynamical mass were derived from SED fitting and kinematics of gas. In the future, we will further develop these results using more clusters to better constrain the derived physical properties.

6.2.2 Expansion to other wavelengths

Furthermore, we will explore an extensive set of multi-wavelength data at intermediate redshift in galaxy clusters. In particular, we will study the relationship between far-infrared luminosity and radio flux density in the rich environment of massive clusters in our universe. This relationship has shown correlation in low redshift clusters but is relatively unexpected at intermediate redshift where we observed an increase in radio sources and star formation in rich galaxy clusters. The physical properties of these star forming galaxies such as star formation rate (SFR) will be mapped as function of galaxy density.

7
Appendix

7.1 Python scripts

This set of script was written to perform least square SEDs fitting. We provide further details in the text below. The script chi2.py calls functions defined in file filter and readfield. The scripts were written using the Python language. They need the third-party tools, numpy, numarray and pylab to be installed.

Fitting code chi2.py

```
#!/usr/bin/python
# importing modules
import sys
from math import *
from numpy import *
import filter
import string
from scipy.io import read_array
# defining some global variables
err_limit=0.2
mag_err_min=0.02
# define calc_norm module
def calc_norm(flux, err, mflux):
    mask=(err/flux < err_limit)
    flux_num=sum(flux[mask]*mflux[mask]/err[mask]**2)
    flux_den=sum(mflux[mask]**2/err[mask]**2)
    norm=flux_num/flux_den
    return norm
    # define calc_chi2 module
def calc_chi2(flux, err, mflux, norm):
```

```
        mask=(err/flux < err_limit)
        chi2=sum((flux[mask]-norm*mflux[mask])**2/err[mask]**2)
        for i in range(len(flux)):
        print flux[i], norm*mflux[i], err[i], (flux[i]-norm*mflux[i])**2/err[i]**2, mask[i]
        return chi2
# define load_object module
def load_object(objfile):
# """read the object file and put it into array"""
        # create id_arr, x_arr, y_arr, z_arr, z_err, mag_arr, mag_err
        z_arr= loadtxt(objfile,usecols=(3,), unpack=True)
        mag_arr= loadtxt(objfile,usecols=(5,7,9,11,13,15), unpack=True)
        mag_err= loadtxt(objfile,usecols=(6,8,10,12,14,16), unpack=True)
        # check to make sure that the magnitude error is reasonable
        # require minimum magnitude error of 0.02
        mag_err=(mag_err**2+mag_err_min**2)**0.5
        # print z_arr, mag_arr, mag_err
        return mag_arr,mag_err,z_arr
# define load_models module
def load_models(modelfile):
        """ Read in the models """
        # read in modelfile to a list
        f=open(modelfile, 'r')
        models_list=f.readlines()
        f.close()
        # read in all models
        model_wave_list=[]
        model_flux_list=[]
        for models_file in models_list:
                # print models_file.strip()
                w, f = loadtxt(models_file.strip(), usecols=(0,1), unpack=True)
                model_wave_list.append(w)
                model_flux_list.append(f)
        return models_list, model_wave_list, model_flux_list
# define load_filters module
def load_filters(filterfile):
        # read in the filters
```

```python
    # read in filterfile to a list
    f1=open(filterfile, 'r')
    filt_list=f1.readlines()
    f1.close()
    for i in range(len(filt_list)): filt_list[i]=filt_list[i].strip()
    # read in all filters
    filt_wave_list=[]
    filt_tran_list=[]
    for filt_file in filt_list:
        w, t = loadtxt(filt_file, usecols=(0,1), unpack=True)
        filt_wave_list.append(w)
        filt_tran_list.append(t)
    return filt_list, filt_wave_list, filt_tran_list
# define chi2 module which will be called in the main argument (sys.argv[])
def chi2(objfile, modelfile, filterfile):
    """Chi2.py is a program to read in cat of objects, list of SEDs and find
the best
    fitting spectra to each object.  The format for the catalog of objects
should be:
    id,x,y,z,z_err, m1, m1_err,...mN, mN_err.
    The task is called by running:
    python chi2.py [object.cat] [list of models] [list of filters] """
    # call load_object module
    mag_arr, mag_err, z_arr = load_object(objfile)
    # for i in range(len(z_arr)):
    # mag_arr=random.normal(mag_arr[i], mag_err[i])
    # all load_models module
    models_list, model_wave_list, model_flux_list=load_models(modelfile)
    # call load_filters module
    filt_list, filt_wave_list, filt_tran_list=load_filters(filterfile)
    # convert magnitude of selected objects to flux
    flux_arr=mag_arr.copy()
    flux_err=mag_err.copy()
    for i in range(len(mag_arr)):
        flux_arr[i]=filter.calc_flux(mag_arr[i], filt_list[i])
        # calculate the error in each band
```

```
        flux_err[i]=mag_err[i]*flux_arr[i]/1.087
    w=zeros(len(filt_list), dtype=float)
    for i in range(len(filt_list)):
        w[i]=filter.central_wave(filt_list[i])
        # calculate the χ² for each object in the objfile
        # first loop over objects
        fout = open("bc2003allchi2Bfit.cat", "w")
        for i in range(len(flux_arr[0])):
            z_red=z_arr[i]
            # calculate χ² value for all models
            # call find_chi2 module
            pick, const=find_chi2(flux_arr[:,i], flux_err[:,i], models_list, model_wave_list,
model_flux_list, filt_list, filt_wave_list, filt_tran_list, z_red)
            # print out the best results for each object
            # find the minimum χ²
            bestmodel_id=pick.argmin()
            print i, z_arr[i], bestmodel_id, pick.min(), pick[bestmodel_id], const[bestmodel_id],
models_list[bestmodel_id]
            fout.write(" %d %s %s %s %s %s %s \n" % (i, z_arr[i], bestmodel_id,
pick.min(),
pick[bestmodel_id], const[bestmodel_id], models_list[bestmodel_id]))
# calculate χ² value for all models
# define find_chi2 module
def find_chi2(flux_arr, flux_err, models_list, model_wave_list, model_flux_list, filt_list,
filt_wave_list, filt_tran_list, z_red):
    pick=zeros(len(models_list), dtype=float)
    const=zeros(len(models_list), dtype=float)
    # for each model, calculate the χ²
    # loop over the models
    for j in range(len(models_list)):
            mod_name=models_list[j]
            mflux_arr=zeros(len(filt_list), dtype=float)
            spec_wave=model_wave_list[j]
            spec_flux=model_flux_list[j]
            # calculate the flux in each filter at the appropriate redshift
                for k in range(len(filt_list)):
```

```
                    mflux_arr[k]=filter.calc_spectra_flux(filt_wave_list[k], filt_tran_list[k],
spec_wave, spec_flux, z=z_red)
                    # calculate the χ² for that model
                    norm=calc_norm(flux_arr, flux_err, mflux_arr)
                    chi2=calc_chi2(flux_arr, flux_err, mflux_arr, norm)
                    pick[j]=chi2
                    const[j]=norm
                    # find the minimum χ²
        return pick, const
if __name__=="__main__":
        if len(sys.argv) < 3:
                print chi2.__doc__
        else:
                objfile=sys.argv[1]
                modelfile=sys.argv[2]
                filterfile=sys.argv[3]
                chi2(objfile, modelfile, filterfile)
```

Bibliography

Alba A. B., Koopmans L. V. E., Garrett M. A., Wucknitz O., & Limousin M., 2010, A&A, 509, A54

Auger M. W., Treu T., Bolton A. S., Gavazzi R., & Koopmans L. V. E. et al., 2010, arXiv:1007.2880v1

Butcher H., & Oemler A., 1978, ApJ, 219, 18, 30

Butcher H., & Oemler A., 1978, ApJ, 226, 559, 565

Butcher H., & Oemler, A., 1984, ApJ, 285, 426, 438

Bundy K., Fukugita M., Ellis R. S., Targett T. A., Belli S., & Kodama T., 2009, ApJ, 697, 1369, 1383

Bundy K., Scarlata C., Carollo C. M., Ellis R. S., Drory N., Hopkins P., Salvato M., Leauthaud A., Koekemoer M. A., Murray N., Ilbert O., Oesch P., Ma C., Capak P., Pozzetti L., & Scoville N., 2009, arXiv: 0912.1077v1

Bundy K., Ellis R. S., Conselice C. J., Taylor J. E., Cooper M. C., Willmer C. N. A., Weiner B. J., Coil A. L., Noeske K. G., & Eisenhardt P. R. M., 2006, ApJ, 651, 120, 141

Bundy K., Treu T., & Ellis R. S., 2007, ApJ, 665, L5, L8

Bundy K., Fukugita M., Ellis R. S., Kodama T., & Conselice C. J., 2004, ApJ, 601, L123, L126

Bundy K., Ellis R. S., & Conselice C. J., 2005, ApJ, 625, 621, 632

Bershady M. A., Vils M., Hoyos C., Guzmán R., & Koo D. C., 2004, arXiv: 0411597v1

Bruzual G., & Charlot S., 2003, MNRAS, 344, 1000, 1028

Bruzual G. & Charlot S., 1993, ApJ, 405, 538, 553

Bartelmann M. (2010), arXiv:1010.3829v1

Bastian N., Covey K. R, Meyer M. R., 2010, arXiv:1001.2965v2

Brinchmann J., & Ellis R. S., 2000, ApJ, 536, L77, L80

Brammer G. B., & Dokkum V. G. P., 2007, ApJ, 654, L107, L110

Boselli A., Boissier S., Cortese L., de Paz A. G., Seibert M., Madore B. F., et al., 2006, ApJ, 651, 811, 821

Boselli A., & Gavazzi G., 2006, arXiv:0601108v1

Borys C., Chapman S., Donahue M., Fahlman G., & Halpern M. et al., 2004, MNRAS, 352, 759, 767

Conroy et al., 2009, ApJ, 699, 486, 506

Cimatti A., Mignoli M., Daddi E., Pozzetti L., et al. (2002), arXiv:0206168v1

Crawford S. M., Bershady M. A., & J. G. Hoessel, 2009, ApJ, 690, 1158, 1180

Charlot S. & Bruzual G., 1991, ApJ, 367, 126, 140

Calzetti D., Armus L., Bohlin R. C., Kinney A. L., Koornneef T., & Bergmann T. S., 2000, ApJ, 533, 682, 695

Crawford S. M., Bershady M. A., Glenn A. D., & Hoessel J. G., 2006, ApJ, 636, L13, L16

Cattaneo A., Dekel A., Faber S. M., & Guierdoni B., 2008, MNRAS, 389, 567, 584

Covone G. & Napolitano N. R., 2004, AN 325, 104, 107

Colina L., Arribas S., & Monreal-Ibero A., 2005, ApJ, 621, 725, 737

Carroll B. W., Ostlie D. A., 'An introduction to modern astrophysics', Pearson Addison-Wesley, 1278P, 2007

Crawford S. M., Bershady M. A., Glenn A. D., & Hoessel J. G., 2004, arXiv: 0401448v1

Cardelli J. A, Clayton G. C, & Mathis J. S., 1989, ApJ, 345, 245, 256

de Jong R. & Bell E., 2006, arXiv:0604391v1

Donahue M. & Stocke J. T., 1995, ApJ, 449, 554, 566

Donahue M., Gaskin J. A., Patel S. K., & Joy M. et al., 2003, ApJ, 598, 190, 209

Donahue M., Voit G. M., Scharf C. A., & Gioia I. M. et al., 1999, ApJ, 527, 525, 534

Drory et al., 2004, ApJ, 616, L103, L106

Deng X. F., 2010, ApJ, 721, 809, 814

Elmegreen B. G., 1997, arXiv:9712352v1

Faber S. M., 1972, ApJ, 20, 361, 374

Fischera J., Dopita M. A., & Sutherland R. S., 2003, ApJ, 599, L21, L24

Garland C. A., Williams J. P., Pisano D. J., Guzmán R., Castander F. J., & Brinkmann
    J., 2005, ApJ, 624, 714, 725

Garland C. A., Pisano D. J., Williams J. P., Guzmán R., & Castander F. J., 2004, ApJ,
    615, 689, 701

Garland C. A., Pisano D. J., Williams J. P., Guzmán R., & Castander F. J., 2003, arXiv:
    0310857v1

Garland C. A., Pisano D. J., Williams J. P., Guzmán R., Castander F. J., & Sage L. J.,
    2007, ApJ, 671, 310, 322

Guzmán R., Östlin G., Kunth D., Bershady M. A., Koo D. C., & Pahre M. A., 2003, ApJ,
    586, L45, L48

Guzmán R., Gallego J., Koo D. C., Phillips A. C., Lowenthal J. D., Faber S. M., Illing-
    worth G. D., & Vogt N. P., 1997, ApJ, 489, 559, 572

Gioia I. M., Maccacaro T., Morris S. L., & Schild R. E. et al., 1988, IAUS, 130, 542G

Gioia I. M. , Maccacaro T. , Schild R. E. , Wolter A., & Stocke J. T. et al., 1990, ApJ,
    72, 567, 619

Giacconi R., Branduardi G., Briel U. & Epstein A. et al., 1979, ApJ, 230, 540, 550

Gioia I. M. & Luppino G. A., 1994, ApJ, 94, 583, 614

Hoyos C., Guzmán R., Diaz A. I., Koo D. C., & Bershady M. A., 2007, ApJ, 134, 2455,
    2473

70

Heavens A., Panter B., Jimenez R., Dunlop J., 2004, arXiv:0403293v1

Holden et al., 2006, ApJ, 642, L123, L126

Henry J. P., Gioia I. M., Maccacaro T., Morris S. L., & Stocke J. T. et al., 1992, ApJ, 386, 408, 419

Haines C. P., Smith G. P., Egami E., & Ellis R. S. et al., 2009, ApJ, 704, 126, 136

Koo D. C., Guzmán R., Gallego J., & Wirth G. D., 1997, ApJ, 478, L49, L52

Kitsionas S., 2003, arXiv:0307478v1

Kriek M., Labbe I., Conroy C., Whitaker K. E., & van Dokkum P. G. et al., 2010, ApJ, 722, L64, L69

Knapen J. H., Mahoney T. J., & Vazdekis A., 2008, ASP, Vol. 390

Knapen J. H., Mahoney T. J., & Vazdekis A., 2008, ASP, 390.

Lowenthal J. D., Durham R. N., Lyons B. J., Bershady M. A, Gallego J., Guzmán R., & Koo D. C., 2005, arXiv: 0502271v1

Le Févre O., et al., 2005, A&A, 439, 877, 885

Lima J. A. S., Holanda R. F. L., & Cunha J. V., 2010, arXiv:1009.2736v1

Maraston C. (1998), MNRAS, 300, 872, 892

Moran S. M, Miller M., Treu T., Ellis R. S., et al., 2007, ApJ, 659, 1138, 1152

Moran S. M, Ellis R. S, Treu T., Smail I., et al., 2005, ApJ, 634, 977, 1001

Massarotti M., Iovino A., & Buzzoni A., 2001, A&A, 368, 74, 85

Moran S. M, Loh B. L., Ellis R. S, Treu T., et al., 2007, ApJ, 665, 1067, 1073

Moran S. M, Ellis R. S., Treu T., Smith G. P., et al., 2007, ApJ, 671, 1503, 1522

Maraston et al., 2006, IAU , 235

McKee C. F., Ostriker E. C., 2007, arXiv:0707.3514v2

Noeske K. G., Koo D. C., Phillips A. C., Willmer C. N. A., & Melbourne J., 2006, ApJ, 640, L143, L146

Noeske et al., 2006, ApJ, 640, L143, L146

Pirzkal N., Xu C., Ferreras I., Malhotra S., Mobasher B., Rhoads J. E., Pasquali A., Panagia N., Koekemoer A. M., Ferguson H. C., & Gronwall C., 2006, ApJ, 636, 582-591

Phillips A. C., Guzmán R., Gallego J., Koo D. C., Lowenthal J. D., Vogt N. P., Faber S. M., & Illingworth G. D., 1997, ApJ, 489, 543, 558

Pérez-Gallego J., Guzmán R., Castillo-Morales A., Castander F. J., Gallego J., Garland C. A., Gruel N., Pisano D. J., Sánchez S. F., & Zamorano J., 2010, MNRAS, 402, 1397, 1406

Pisano D. J., Garland C. A., Rabidoux K., Wolfe S., Guzmán R., Pérez-Gallego J., & Castander F. J., 2009, arXiv: 0912.3283v1

Pisano D. J., Garland C. A., Guzmán R., Pérez-Gallego J., Castander F. J., & Gruel N., 2007, arXiv: 0712.1243v1

Polletta, et al., 2007, ApJ, 663, 81

Padmanabhan N., Seljak U., Strauss M. A., Blanton M. R., et al. (2003), arXiv:0307082v1

Pickles A. J., 1985, ApJ, 59, 33, 61

Padmanabhan N., Seljak U., Strauss M. A, Blanton M. R., & Kauffmann G. et al., 2003, arXiv:0307082v1

Padmanabhan T. (2003), arXiv:0212290v2

Pipino A., Silk J., & Matteucci F., 2008, MNRAS, 000, 000-000

Pipino A., Silk J., & Matteucci F., 2008, Astron, 000, 000-000.

Poggianti B. M., Smail I., Dressler A., Couch W. J., et al., 1999, ApJ, 518, 576, 593

Poggianti B. M., Desai V., Finn R., Bamford S., et al., 2008, ApJ, 684, 888, 904

Rettura A., Rosati P., Strazzullo V., Dickinson M., A&A, 458, 717, 726

Reese E. D., Mohr J. J., Carlstrom J. E., Joy M., & Grego L. et al., 2000, ApJ, 533, 38, 49

Rigby J. R., Marcillac D., Egami E., Rieke G. H., & Richard J. et al., 2008, ApJ, 675, 262, 280

Shu F. H. , Adams F. C., & Lizano S., 1987, ARA&A, 25, 23S

Stocke J. T., Morris S. L., Gioia I. M., & Maccacaro T. et al., 1991, ApJ, 76, 813, 874

Stanford S. A., Eisenhardt P. R., Dickinson M., Holden B. P., & De Propris R., 2002, ApJ, 142, 153, 160

Shan H. Y., Qin B., & Zhao H. S, 2010, MNRAS, 408, 1277, 1282

Scalo J. M., 1986, IAUS, 116, 451S

Stoughton C. (2002), ApJ, 123, 485, 548

Sato T., & Martin L., 2006, ApJ, 647, 946, 969

Saintonge A., Tran K. H., Holden B. P., 2008, ApJ, 685, L113, L116

Tollerud E. J., Barton E. J., Zee L. V., & Cooke J., 2010, ApJ, 708, 1076, 1091

Tripicco M. J. & Bell R. A., 1995, AJ, 110, 3035T

Tran et al., 2005, ApJ, 619, 134, 146

Vigroux L., Boulade O., & Rose J. A., 1989, ApJ, 98, 2044V

Vergani D., et al., 2008, A&A, 487, 89-101

Vazdekis A., Casuso E., Peletier R. F., & Beckman J. E., 1996, ApJ, 106, 307, 339

Vallenari A., Tantalo R., Portinari L., & Moretti A., 2007, ASP, Vol. 374

Van der Wel et al., 2006, ApJ, 652, 97, 106

Walcher J., Groves B., Budavari T., & Dale D., 2010, arXiv:1008.0395v1

Wardlow J. L., Smail I., Wilson G. W., Yun M. S., Coppin K. E. K., Cybulski R., & Geach J. E. et al., 2010, MNRAS, 401, 2299, 2317

Werk J. K., Jangren A., & Salzer J. J., 2004, ApJ, 617, 1004, 1016